CORRELATION BETWEEN ATOMIC-SCALE STRUCTURES AND MACROSCOPIC ELECTRICAL PROPERTIES OF METAL-COVERED Si(111) SURFACES

SHUJI HASEGAWA[a,b] and SHOZO INO[a]

[a]*Department of Physics, Faculty of Science, University of Tokyo, Hongo, Bunkyo-ku, Tokyo 113, JAPAN*

[b]*PRESTO, Research Development Corporation of Japan (JRDC)*

In this review, we discuss the relation between the atomic-scale structures (atomic arrangements and electronic states) and the macroscopic electrical properties (surface conductance and Schottky barriers) of metal(Ag, Au, or In)-covered Si(111) surfaces. These surfaces have been one of the most intensively investigated systems with the use of a variety of modern surface science techniques, and diversified information at atomic scales has been obtained. The data of reflection high-energy electron diffraction, scanning tunneling microscopy/spectroscopy, photoemission spectroscopies, and others are utilized here for characterizing the structures. Surface conductance and Schottky barriers, on the other hand, have also been the major areas in semiconductor physics for, especially device-oriented, research, but these have rarely been studied in combination with atomic-scale structures. These electrical properties have recently been found to be crucially dependent on the local atomic structures of well-defined surfaces/interfaces. The atomic arrangements and the resulting surface/interface electronic states govern the Fermi-level pinning and band bending which determine the electrical properties of semiconductor surfaces/interfaces.

1. Introduction

A variety of recent experimental techniques in surface science provide diversified information on the atomic and electronic structures of solid surfaces/interfaces at atomic scales. Generally accepted structural models for Si(111)-7×7 and Si(100)-2× 1($-c(4\times2)$) surfaces, for example, have now been confirmed after long controversies.[1] The former structure has been finally solved by a transmission electron diffraction (TED) method as a "dimer-adatom-stacking fault (DAS)" structure,[2] and the electronic state corresponding to each atomic bonding in the unit cell has been assigned by photoemission spectroscopies[3] and "current imaging tunneling spectroscopy".[4] The Si(100) surfaces are consistent with buckled dimer structures. Another puzzling surface, Si(111)-$\sqrt{3} \times \sqrt{3}$-Ag structure has also been settled down to be a "honeycomb-chained trimer (HCT)" structure, solved by X-ray diffraction.[5,6]

These experimental methods have been utilized not only for structure analysis, but also for the control of epitaxial growths of thin crystals with monolayer precision. Especially, in addition to the observations of long-range orders in geometrical structures, reflection high-energy electron diffraction (RHEED) is widely used for *in situ* monitoring in molecular beam epitaxy (MBE) through the intensity oscillations of its specular beam during growths.[7] Furthermore, remarkable demonstrations of "single-atom manipulation" was carried out with scanning tunneling microscope (STM) technique, suggesting a possibility of structure control on ultimate atomic scales.[8,9]

In this way, the analysis and control of atomic and resulting electronic structures of surfaces/interfaces have now been within our scope. Then, a simple question arises: how do the differences in atomic-scale structures influence their macroscopic properties (electrical, optical, and magnetic properties)? For example, characteristics of Schottky barriers of metal-semiconductor interfaces, surface conductance of semiconductors, photoconduction, tunnel junction, and others must be dependent on the atomic and electronic structures at the surfaces/interfaces. It is, then, of great importance to measure the macroscopic properties of well-defined samples, of which atomic-scale structures should be characterized with the modern surface science techniques. In particular, simultaneous and *in situ* measurements both of the structures and properties in ultra high vacuum environment are highly desirable. The correlation with the microscopic (atomic-scale) structures and macroscopic properties of surfaces/interfaces is one of the most important subjects for fundamental as well as practical interests.

Although the rectifying action of metal-semiconductor contacts has been known for more than a hundred years, the Schottky barrier formation is still a subject of much debate.[10-12] In the original theory of Schottky[13] and Mott,[14] the barrier is formed by a charge flow compensating the work-function difference between the metal and semiconductor. But most of the real contacts do not follow this theory, because of electronic states localized at the interface to pin the Fermi level. These interface states are sensitively dependent on the detailed atomic structures at the interface. The main dispute at present[15] is the origin of these states: metal-induced gap states (MIGS),[16] or defect states,[17,18] or both.[19] For studies from this point of view, the Schottky barrier height should be measured with well-defined interfaces in atomic and electronic structures. Several experiments with $NiSi_2/Si$,[20] metal/GaAs,[21] Pb/Si,[22-24] and Ag/Si[25] have demonstrated the dominant role of the intrinsic interfacial electronic structures over the macroscopic bulk parameters, playing in determination of the barrier height.

Surface conductivity of semiconductors has also been one of the main subjects in semiconductor physics, especially in its early days.[26-28] But in spite of a great number of studies on this properties, it was not until recently that much attention was paid to the relation between the conductivity and the atomic structures of surfaces. It was demonstrated that, at initial stages of metal depositions onto

Si(111) surface, the conductance parallel to the surface changed crucially depending on the substrate-surface structures.[29-32] This is attributed to the difference in surface space-charge layers in Si substrate, governed by the microscopic electronic surface states.

In the present article, we review measurements of structure-dependent electrical properties, i.e., surface conductance, Hall effect and Schottky barrier height, with several selected metal-Si(111) systems of which atomic and electronic structures are well characterized. The results on the former two properties measured by the authors are mainly described. These macroscopic properties are discussed in connection with the data on microscopic geometric and electronic structures obtained by RHEED observations, valence and core-level photoemission spectroscopies, light reflectance spectroscopy, STM, and others.

The next section is devoted to brief reviews on the nature of the clean Si(111)-7 × 7 surface, and fundamentals of Schottky barriers and surface conductance of semiconductors, on which the discussions in the following sections are based. After that, we go into details of each metal-Si pair, Ag/Si (Sec. 3), Au/Si (Sec. 4), and In/Si (Sec. 5). These pairs have not been chosen to achieve a certain completeness of the works in this area, but rather an overview on this subject with growing interests is provided. The readers should refer to the cited literature for more information.

2. Backgrounds

2.1. *A clean Si(111)-7×7 surface*

It is appropriate at this stage to make a brief summary of our knowledge of the structure and surface electronic states of a clean Si(111)-7 × 7 surface. Comprehensive reviews on this surface are given, for example, by Haneman.[1,33]

Figure 1 shows the atomic arrangement of the DAS model by Takayanagi *et al.*[2] The lozenge of the 7 × 7-unit cell has corner vacancies which are connected to each other with "chains" of dimers. This unit cell is regarded as containing two triangles separated by the dimer chains. Each triangle has six adatoms (the biggest filled circles) and three "rest atoms" (the medium-sized filled circles), arranged locally in 2 × 2 periodicity. The left and right triangles have the opposite stacking sequences; the left side has a stacking fault (faulted half), while the right does not (unfaulted half). This structure has 19 dangling bonds, which is a significant reduction in the number of unpaired electrons from 49 at an ideal unreconstructed (111) surface. This leads to a decrease of the total energy, which is, however, balanced against an energy increase caused by large angular strains of unusual bondings. The reduction of the energy from the ideal unrelaxed surface was theoretically estimated to be 0.36 eV[34] or 0.40 eV[35] per 1 × 1 unit.

Figure 2(a) shows a RHEED pattern from the Si(111)-7 × 7 surface.[36] A fine electron beam of 15 kV acceleration irradiated the surface in [11$\bar{2}$] incidence with glancing angle of 3.1°. It has now been established that the sample, commercially-

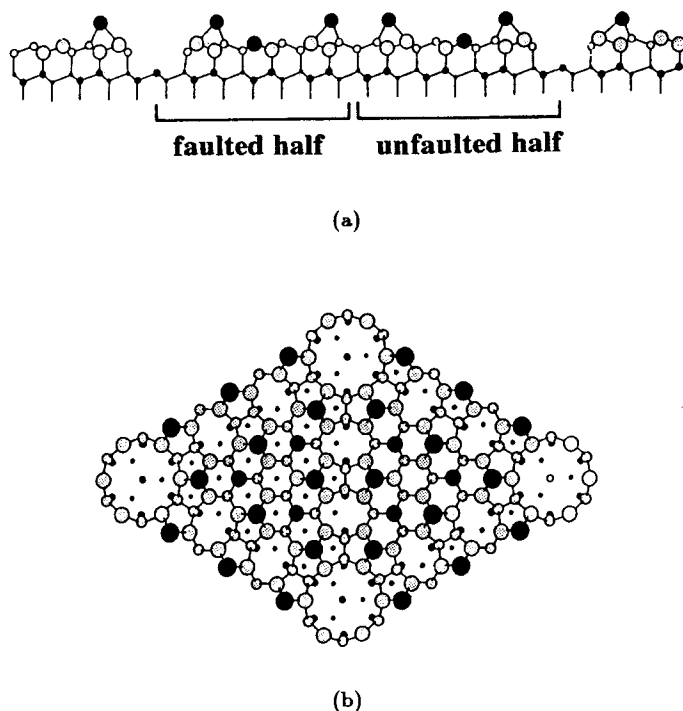faulted half   unfaulted half

(a)

(b)

Fig. 1. A schematic illustration of the DAS (dimer-adatom-stacking fault) model for a clean Si(111)-7 × 7 reconstruction as proposed by Takayanagi et al.[2] (a) side view (a section through the long diagonal of the unit cell) and (b) top view.

obtained mirror-polished Si single-crystal wafer, can be cleaned only by several flash heatings up to 1200°C in ultra high vacuum (UHV) environment. Such a high temperature is needed to eliminate ambient contamination, especially carbon. Heating at 1200°C also permits the removal of previously deposited metals (Ag, Au, Pb, In, etc.) and the re-use of the silicon wafer for the next measurements. A low temperature thermal cleaning method for Si wafers has been proposed by Ishizaka and Shiraki[37] which consists of wet chemical treatment and heating below 800°C in UHV. This method also enables us to prepare contaminants-free surfaces. The clean surface shows a 1 × 1 pattern without superlattice reflections above around 830°C (Fig. 2(b)) which transformed into the 7×7 pattern (a) by slowly cooling down. This structural phase transition is reversible and of first order.[127] The fractional-order spots of $(\frac{3}{7}, 0)$, $(\frac{4}{7}, 0)$, $(\frac{3}{7}, \frac{1}{7})$, $(\frac{4}{7}, -\frac{1}{7})$, and equivalent ones in the RHEED pattern (a) are known to be stronger than other superlattice reflections due to the interference of waves scattered from adatom-arrays of 2 × 2 periodicity.[38] This feature, which is a qualitative sign of cleanliness of the surface, disappears when foreign atoms such as metals and residual gases adsorb on the surface.[39–41]
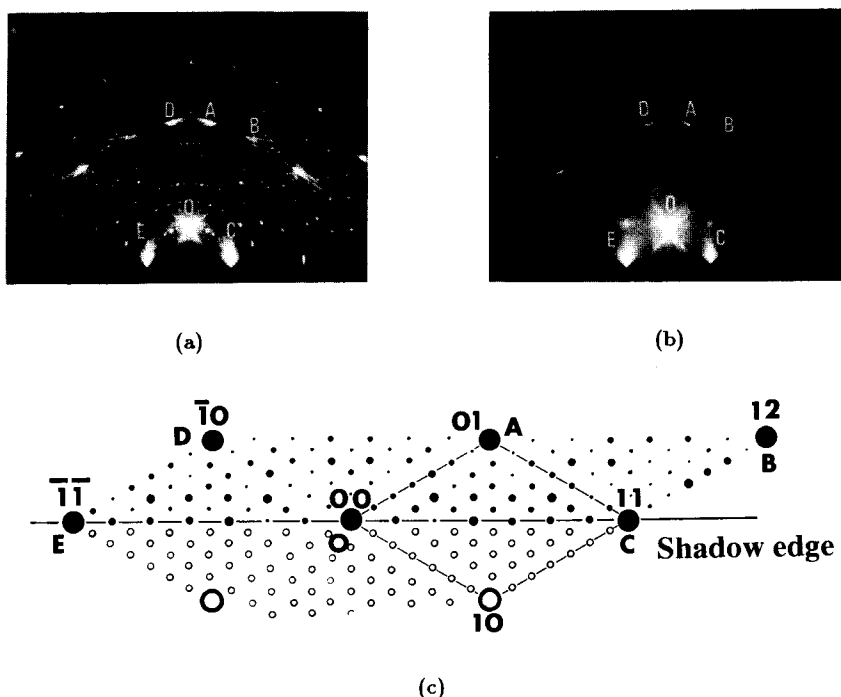
(a)

(b)

(c)

Fig. 2. RHEED patterns from a clean Si(111) surface showing (a) the 7 × 7 structure at room temperature, and (b) a 1 × 1 structure at 850° C in [11$\bar{2}$] incidence. (c) Two-dimensional reciprocal lattice for (a).

Figure 3(a) shows angle-integrated ultraviolet photoemission spectra from Si(111)-7 × 7 at 300 K (upper panels) and 20 K (lower panels).[42] Surface state peaks are marked by vertical lines, which are identified by noting their disappearance after H adsorption. Three conspicuous surface states S_1, S_2, and S_3 are recognized around 0.2, 0.9, and 1.8 eV, respectively, below the Fermi level. These states are now identified with particular sites in the 7 × 7 unit cell by current imaging tunneling spectroscopy (CITS) with changing the tip bias of STM.[4] S_1 peak is assigned to the dangling bond state on the 12 adatoms of the DAS structure. Since this state extends to the Fermi level, it is considered to be half occupied, i.e., a metallic state. S_2 peak originates from the dangling bond state on the 6 remaining atoms of the first full atomic layer which are not bonded to the adatoms. S_3 state, called a backbond state, is assigned to the bonding state between the adatoms and the first layer atoms. These assignments are also supported by theoretical calculations.[34,43]

The Fermi level is considered to be pinned at the metallic S_1 state due to its high density of states. Its position E_F with respect to the valence band maximum E_{VBM} at this surface was measured to be $E_F - E_{VBM} = 0.63 \pm 0.05$ eV from core-level photoemission data.[44] Since this position is around the middle of the band gap, the
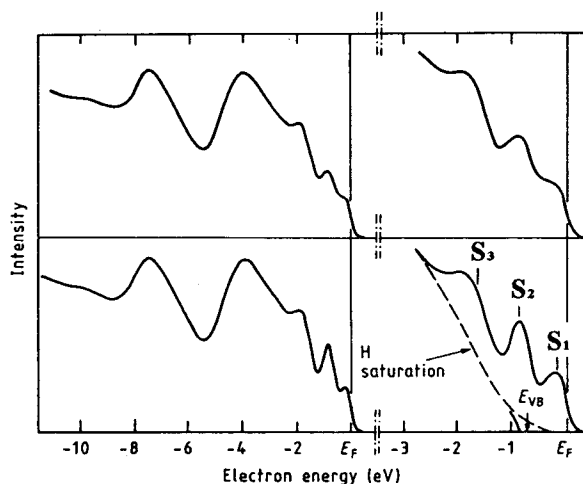
(a)
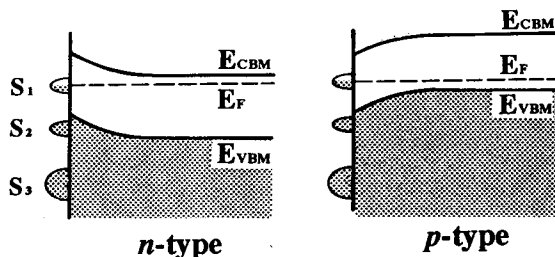
(b)

Fig. 3. (a) Angle-integrated ultraviolet photoemission spectra ($h\nu = 21.2\,\text{eV}$) for Si(111)-7 × 7 at 300 K (upper panel) and 20 K (lower panel).[42] The right panels show an expanded view of the surface states near the top of the valence band. The labels for surface states have been changed from those in the original paper of Demuth *et al.*[42] (b) Schematic energy-band diagrams beneath the 7 × 7 surfaces for *n*-type and *p*-type Si wafers.

surface space-charge layer beneath the 7 × 7 structure always exhibits a depletion layer, irrespective of doping type of the bulk Si (Fig. 3(b)).

2.2. *Schottky barriers*

Since detailed descriptions on the Schottky barriers are found in standard textbooks and comprehensive reviews on semiconductor physics and devices,[11,12,45] we are limited here to the role of surface/interface states playing in barrier formation.[46] Two limiting cases are illustrated as energy-band diagrams of metal-*n*-type semiconductor contacts in Fig. 4. In the absence of surface/interface states, as first considered
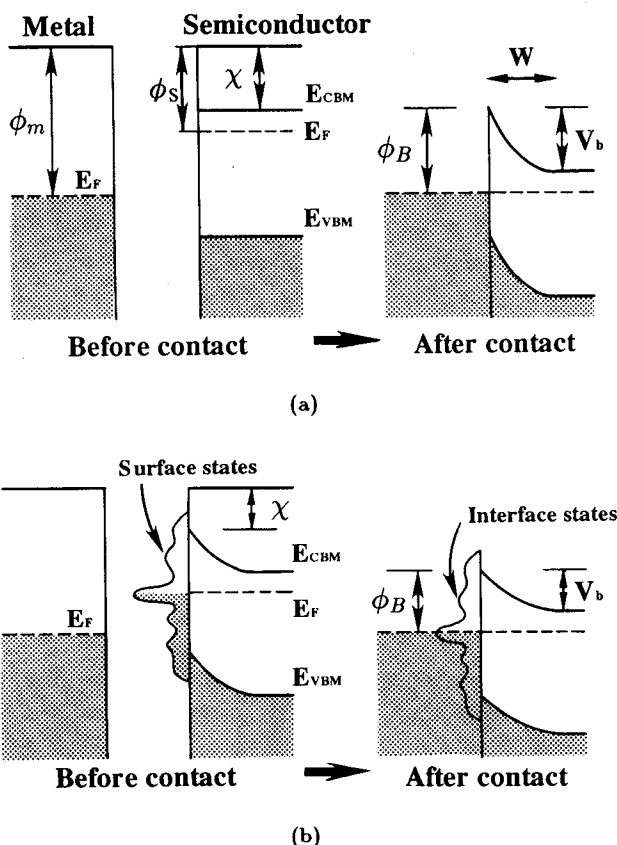
Fig. 4. Energy-band diagrams of metal-semiconductor contacts: (a) without, (b) with surface/interface states.

by Schottky[13] and Mott[14] (Fig. 4 (a)), when a metal (work function ϕ_m) and a semiconductor (work function ϕ_s) come into contact ($\phi_m > \phi_s$), the charge will flow from the semiconductor to the metal across the interface, so that the Fermi levels E_F on both sides line up. An extra negative charge is built up on the metal surface in a region of the order of the Thomas-Fermi screening length ($\sim 0.5\,\text{Å}$), while an equal and positive charge (ionized donors) exists in the semiconductor which is distributed over a space-charge region of width W (order of $1000\,\text{Å} \sim 1\mu\,\text{m}$) because of the relatively low carrier concentration. In this case, the Schottky barrier height ϕ_B is simply the difference between the metal work function ϕ_m and the electron affinity χ of the semiconductor,

$$\phi_B = \phi_m - \chi \,, \tag{1}$$

which is only a property of the pairs of materials. The barriers with ionic semi-conductors (e.g., II-VI compounds) tend to obey this Schottky-Mott rule, whereas covalent semiconductors do not.

Another limiting case (Fig. 4(b)) is a model of Bardeen[47] which assumes a dominant role of surface/interface states for the determination of barrier height. Before contact, the surface states of the semiconductor are occupied to a level E_F. After contact and reaching in equilibrium, E_F of the semiconductor falls an amount equal to the contact potential by a redistribution of charge. The neutrality condition that the negative charge on the metal side must be equal and opposite to the positive charge due to the uncompensated donors in the semiconductor has to be modified by the charge occupying the surface/interface states. If the density of the surface states is sufficiently large to accommodate any additional surface charges without appreciably altering the occupation level E_F, the space charge and resultant band bending in the semiconductor will remain unaffected. This means that the Schottky barrier height is determined only by the property of the semiconductor surface and is independent of the particular metal forming the contact. This results from the Fermi-level pinning.

Following Hibma *et al.*,[15] different types of interface states for Fermi-level pinning are illustrated in Fig. 5. In the left-hand panels, the local density of states at the interface (I-LDOS) is shown as a function of the energy in the semiconductor band gap. In the right-hand panels, the dependence of the Schottky barrier height on metal work function is sketched. All available models of Schottky barrier formation fall into one of the following four types:

(a) No pinning states. This is the original treatment of Mott and Schottky, mentioned above (Fig. 4(a)), The slope of the ϕ_B versus ϕ_m is unity in this case.

(b) Continuum of interface states. Metal-induced gap states (MIGS) model[16] belongs to this category, which originate from the wave-function tails of the metal electrons in the energy region of the semiconductor band gap. This model predicts a linear relationship of the barrier height ϕ_B on the metal work function ϕ_m, as does the Schottky-Mott rule, but with a slope of less than unity. This is because much more charge has to be transferred across the interface for Fermi-level shift.

(c) Discrete interface states. In the unified defect model,[17,18,48] the Fermi level is supposed to be pinned by a energy level, which originates from defects created during the interface formation. If the density of defect states is high enough, e.g., of the order of 0.1 state per interface atoms, the Fermi-level position will be almost independent of metal work function ϕ_m within a certain range. Outside this range of ϕ_m, the defect interface states are either completely filled or empty, and the Schottky-Mott rule applies.

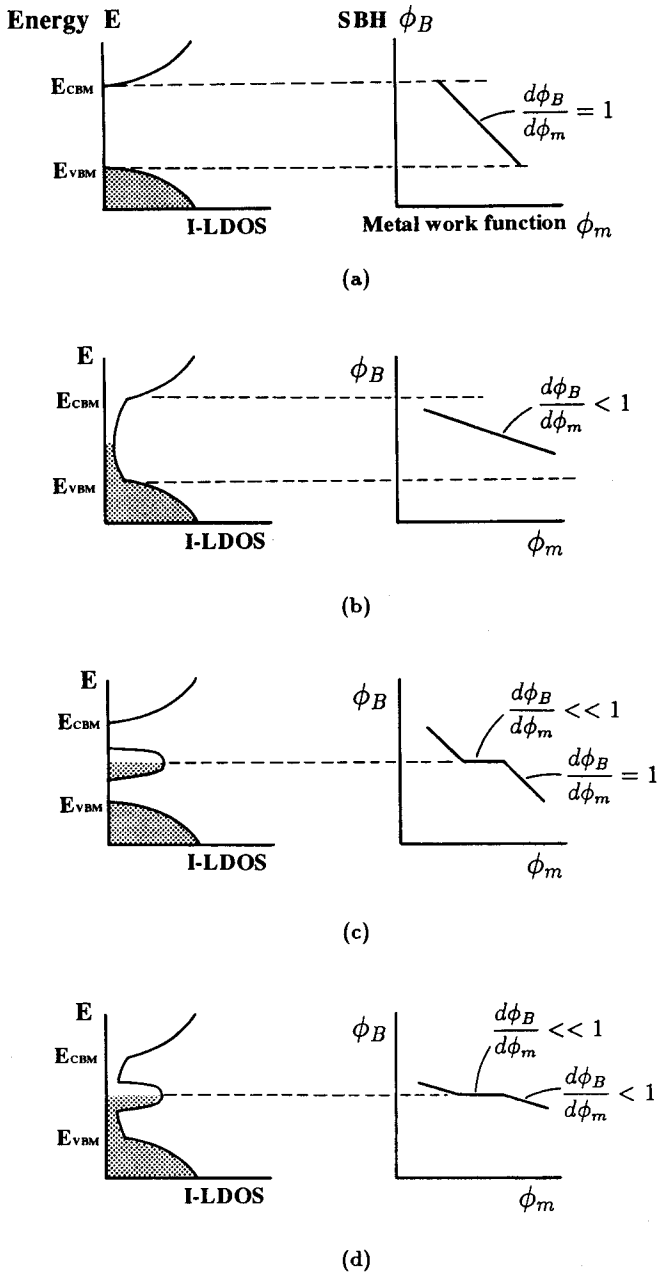(d) Combination of cases (b) and (c).[19]

Fig. 5. The models on Schottky barrier formation can be classified according to the presence and nature of the states that are responsible for Fermi-level pinning at the metal/semiconductor interface.[15] The dependence of the Schottky barrier height ϕ_B on metal-work function ϕ_m is very different if the pinning levels are absent (a), form a continuum (b), form a discrete set of states (c), or both (d). In Ref. 15, the figures are drawn in terms of the metal electronegativity instead of the metal work function.
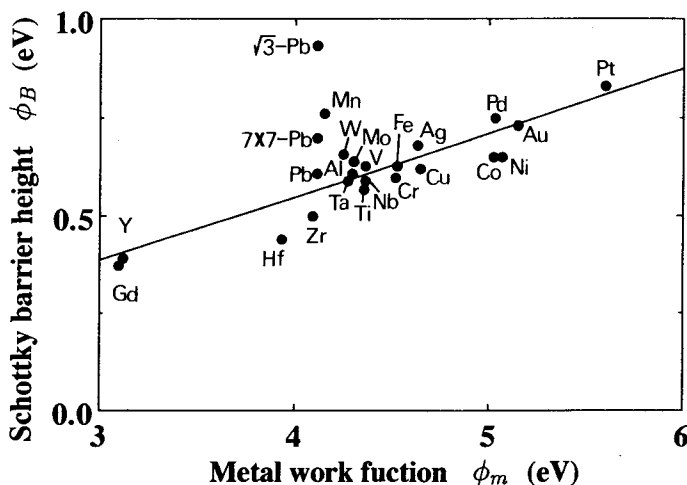
Fig. 6. Schottky barrier heights ϕ_B versus the metal work function ϕ_m for metal-n-type-Si contacts. Values of ϕ_B are collected from.[12,23] Metal work-function data are after Michaelson.[49,50] The labels "$\sqrt{3}$-Pb" and "7 × 7-Pb" indicate the Pb-Si contacts made on Si(111)-$\sqrt{3}$ × $\sqrt{3}$-Pb and clean Si(111)-7 × 7 surfaces respectively.[23]

Figure 6 shows the experimental values of the Schottky barrier height as a function of the metal work-function for n-type Si.[23,49,50] For Si-metal diodes, the trend is nicely predicted by the MIGS model, but does not obey the Schottky-Mott rule. However, the barrier heights of Pb-Si contacts are significantly dependent on the interface structures.[23] A contact of Pb/Si-$\sqrt{3}$ × $\sqrt{3}$-Pb is a clear exception as shown in the figure. Furthermore, since the reactivity with Si is quite different from one metal to another (Au and Ni are known to be highly reactive even at room temperature while Ag and Pb do not), it is obviously inadequate to discuss the barrier height only with work functions of metals. In this paper we address the importance of the local atomic structure at the interface for governing the Schottky-barrier height (SBH). But we must carefully check whether the difference in SBH is intrinsically related to the different interfacial atomic arrangements, or just related to a difference in defect density. This issue is investigated in detail for NiSi$_2$/Si(111) interface.[51]

Experimentally, the Schottky barrier height is determined from current-voltage (I-V), capacitance-voltage (C-V), or photoresponse (I-$h\nu$) characteristics of the diodes. Measurements of substrate core-level shifts in soft X-ray photoemission spectroscopy are also used to determine the Fermi-level position at the interface and the resulting barrier height. This technique, however, is available only in metal coverages of monolayer region because of the short escape depth of photoelectrons. This fact causes a debate on the difference in the barrier heights between the photoemission-spectroscopy measurements and conventional electrical measurements, because the latter methods are for the contacts with thicker metal,

of which the interface structures can be different from the contacts of monolayer metal-coverage used in the former measurement methods.[52-54] Anyway, it is essentially important to measure the Schottky barrier heights with metal-semiconductor contacts, of which interface structures are well characterized.

2.3. *Surface conductance of semiconductors*

. When two electric leads are connected onto a semiconductor surface and a voltage is applied between them, most of the current flows in the interior bulk of the semiconductor in most cases. But under special conditions where the conductivity of the surface region is extremely higher than that of the bulk, the current preferentially passes through near the surface. The measured conductance g of a square piece of arbitrary side length and thickness d has contributions from bulk and surface:

$$g = g_0 + \Delta\sigma , \qquad (2)$$

where g_0 is the bulk contribution $g_0 = \sigma_B \times d$ (σ_B is bulk conductivity) and $\Delta\sigma$ describes the extra contribution from surface region. Three types of electron transport near surface region are possible:

(1) Conduction through a space-charge layer of the semiconductor substrate.
(2) Conduction via surface states. Since surface states on periodic surfaces form two-dimensional bands, electrons should be mobile along the surface like electrons in the bulk bands. The type of conductivity may be metallic, semiconducting, or insulating, depending on the surface-state band structure and Fermi-level position. Although their conductivities were estimated by Henzler,[28] any unambiguous experimental results of surface-state conductivity have not yet reported.
(3) Conduction through a grown adsorbate layer, for example, a metal layer grown on a semiconductor surface. This type of conduction may be set on at metal coverages enough to make percolation paths.

We mainly discuss the first conduction mechanism. Various kinds of electronic devices such as field-effect transistors (FET) work on the basis of the controllability of the surface conductance of the space-charge layer. The surface conductivity is proportional to the product of carrier density and mobility in the surface space-charge region. The mobility is determined by various kinds of scattering processes of carriers and their effective masses, which are discussed in detail in textbooks.[26-28] We focus our attention here only to the carrier-density changes relating to the band bending at surfaces.

Figure 7(a)-(d) shows schematic band diagrams at four different situations of surface space-charge layer for an *n*-type semiconductor: (a) an accumulation layer, (b) flat band condition, (c) a depletion layer, and (d) an inversion layer. These conditions are realized by applying an external electric field normal to the surface or introducing appropriate surface states. The excess surface-carrier densities due
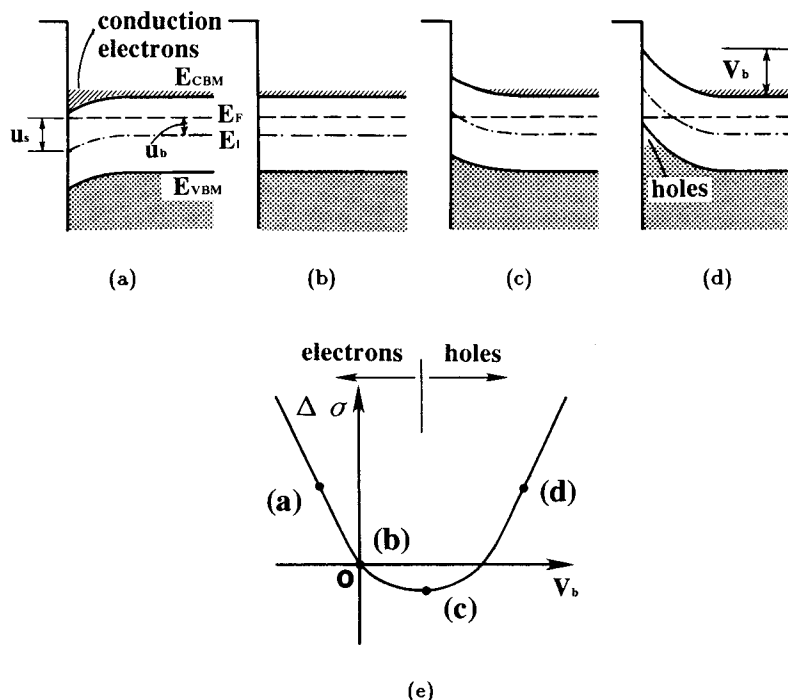
Fig. 7. Energy-band diagrams indicating four different situations of the surface space-charge layer of an n-type semiconductor: (a) an accumulation layer, (b) flat band condition, (c) a depletion layer, and (d) an inversion layer. (e) An illustration showing the relation between surface conductance $\Delta\sigma$ and surface potential V_b.

to the band bending are defined as the number (per unit surface area) of mobile electrons, Δn, and holes, Δp, in the space-charge layer with respect to those under flat band condition ($V_b = 0$, i.e., Fig. 7(b)). This definition is expressed as

$$\Delta n = \int_0^\infty (n(z) - n_b)dz , \quad \Delta p = \int_0^\infty (p(z) - p_b)dz , \qquad (3)$$

where $n(z)$ and $p(z)$ are concentrations of carriers, electrons and holes, respectively, at a depth of z from the surface (z-axis is normal to the surface towards the interior). n_b and p_b are constants of carrier concentrations in the inner bulk. By solving Poisson's equation, the surface excess-carrier concentrations are obtained as

$$\Delta n = n_i L_D \cdot G(-u_s, -u_b) , \quad \Delta p = n_i L_D \cdot G(u_s, u_b) , \qquad (4)$$

where n_i is the intrinsic carrier density and L_D the Debye length. The function $G(u_s, u_b)$ is tabulated and illustrated in Refs. 26, 27, 55, 56 as a function of $u_b = (E_F - E_i)/kT$ and $u_s = (E_F - E_i)/kT$ at surface (see Fig. 7(a)). Then the surface
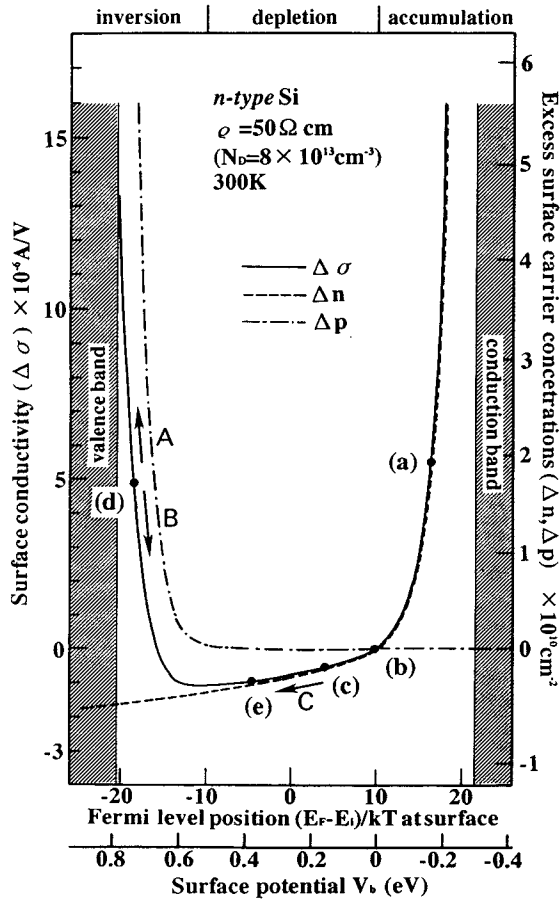
Fig. 8. Calculated excess surface-carrier concentrations (Δn and Δp) and surface conductivity $\Delta\sigma$ as a function of surface potential V_b for an n-type Si with doping concentration $N_D = 8 \times 10^{13}\,\mathrm{cm}^{-3}$ at 300 K using the graphs by Young.[55] The intrinsic carrier density $n_i = 1.5 \times 10^9\,\mathrm{cm}^{-3}$ [45] and the Debye length $L_D = 23.3\,\mu\mathrm{m}$.[56] The points (a) $\sim$ (d) on the $\Delta\sigma$-curve correspond to the respective conditions in Fig. 7. Especially, the point (c), located at 0.63 eV above the valence-band maximum E_{VBM}, indicates the E_F positions at the Si(111)-7 $\times$ 7 surface. The point (d) roughly represents the E_F positions at the Si(111)-$\sqrt{3} \times \sqrt{3}$-Ag surface (Sec. 3) and the Au-induced-superstructure surfaces (Sec. 4), but their accurate positions are not determined.

conductance $\Delta\sigma$ at any surface potential V_b is defined as

$$\Delta\sigma = e(\mu_n \Delta n + \mu_p \Delta p) \,, \tag{5}$$

where μ_n and μ_p are mobilities of electrons and holes respectively in the space-charge region. Figure 8 shows the calculated variation of surface conductance $\Delta\sigma$ as a function of surface potential (band bending) V_b. The minimum conductance

corresponds to the condition of depletion layer Fig. 7(c). In the right-hand branch of the curve, the surface conductance arises mainly from electrons (Δn) in the conduction band (an accumulation layer), while in the left-hand branch, from holes (Δp) in the valence band (an inversion layer). In the vicinity of the minimum, $\Delta\sigma$ consists of contributions from both electrons and holes. $\Delta\sigma$ becomes zero twice; one for the case of flat bands $V_b = 0$ (Fig. 7(b)) by definition, and the other corresponds to the condition where the hole conductance just cancels the negative contribution of the depleted majority carrier, electrons.

Then, a given semiconductor is regarded as two conductors in parallel, one associated with the fixed carrier density in the underlying bulk, and the other with the surface-potential-dependent carrier concentration in the space-charge layer. In most cases only *changes* in the conductance at the space-charge layer can be experimentally measured directly.

The most common method for measuring resistance is the four-point probe method.[45] A small current I from a constant-current source is passed through the outer two probes and the voltage V is measured between the inner two probes. The sheet resistance R_s is given by

$$R_s = \frac{V}{I} \cdot \mathrm{CF} \quad (\Omega/\text{square}) , \tag{6}$$

where CF is the correction factor.[57] The resistivity is then

$$\rho = R_s d \quad (\Omega \cdot \text{cm}) , \tag{7}$$

where d is the thickness of the wafer. For semiconductors with both electrons and holes as carriers,

$$\rho = \frac{1}{e(\mu_n n + \mu_p p)} , \tag{8}$$

and for n-type and p-type semiconductor,

$$\rho = \frac{1}{e\mu_n n} , \quad \rho = \frac{1}{e\mu_p p} , \tag{9}$$

respectively. Thus we can obtain the impurity concentration (=carrier concentration, n or p) in a semiconductor if its resistivity is known.

The surface conductance $\Delta\sigma$ is given by

$$\Delta\sigma = \frac{1}{R_s} - \frac{1}{R_{s0}} \quad (mho) , \tag{10}$$

where R_{s0} is the value of R_s under the flat-band condition $V_b = 0$.

To measure the carrier concentration directly, the most common method uses the Hall effect.[45] In the case of uniform current distribution in the sample, the Hall

coefficient R_H is given by

$$R_H = r \frac{1}{e} \frac{p - b^2 n}{(p + bn)^2} , \quad b \equiv \frac{\mu_n}{\mu_p} , \tag{11}$$

where the Hall scattering factor r lies between 1 and 2. For n-type and p-type semiconductors,

$$R_H = -\frac{r}{en} , \quad R_H = \frac{r}{ep} , \tag{12}$$

respectively. Thus the carrier concentration (n or p) and carrier type (electron or hole) can be determined from the Hall measurements provided that one type of carrier dominates.

In the case of an inhomogeneous sample such as one under the band bending at a surface, we need a general expression for the effective Hall coefficient in terms of parallel conducting slabs within each of which current flows uniformly. From a simple two-layer model,[57] the apparent Hall coefficient is

$$R_H = \frac{R_{Hb} \sigma_b^2 d_b + R_{Hs} \sigma_b^2 d_s}{\overline{\sigma}^2 d} , \tag{13}$$

where the apparent conductivity $\overline{\sigma}$ is

$$\overline{\sigma} = \frac{\sigma_s d_s + \sigma_b d_b}{d} , \tag{14}$$

d_s and d_b being the thicknesses of the surface and the underlying bulk layers, σ_s and σ_d the conductivities, and R_{Hs} and R_{Hb} the Hall coefficients, respectively. Thus errors in the determination of carrier concentration can clearly be serious when the contributions from the surface layer and the bulk are comparable. And, in practice, it is difficult to make the correction with confidence because the surface potential is rarely known accurately.

Brattain and Bardeen[58] found that the surface potential (band bending) V_b can be varied in a reproducible way by exposing the surface cyclically to different gaseous ambients (Brattain-Bardeen cycle). Since their experiments were not carried out with clean semiconductor surfaces in UHV environment, the gases adsorb on the outer surface of the oxide film on the semiconductor in a form of ions, of which electric fields penetrate into the space-charge region across the oxide layer. Morrison[59,60] measured changes in surface conductance in the ambient cycle. Separation of bulk and surface contributions is thus achieved effectively by varying the surface potential and following the resulting change in the conductance of the bulky sample.

The band bending at the semiconductor surface is determined from the neutrality condition that the space-charge (ionized impurities) cancels the charge trapped at the surface electronic states. Then, the changes in the surface states distribution,

originated from the rearrangements of surface atoms, may cause the variations in the band bending and resultant surface conductance.

Changes in surface conductivity accompanying the structural conversions were measured by Mönch and co-workers[61-64] with clean Si and Ge. A Si(111) surface prepared by cleavage in UHV at room temperature is known to exhibit a 2 × 1 structure, of which structural models are still controversial.[1] This structure undergoes an irreversible conversion into the 7 × 7 structure upon heating at around 350° C. Mönch *et al.* carried out LEED(low-energy electron diffraction) observations and simultaneous surface-conductivity and work-function measurements with clean cleaved Si(111) surface as a function of annealing temperatures. Figure 9(a) shows their result which indicates a strong correlation between structural conversion and the change in surface conductivity. In the transient temperature range of 350-400° C for structural transformation from the 2 × 1 to the 7 × 7, the conductivity shows a temporary steep decrease. Using a surface-conductivity-vs-band bending curve like Fig. 8, the conductivity data is transformed into variation of surface potential V_b as shown in Fig. 9(b). The band bending changes depending on the charge in the surface states which redistributes with reconstructions of surface atomic structures.

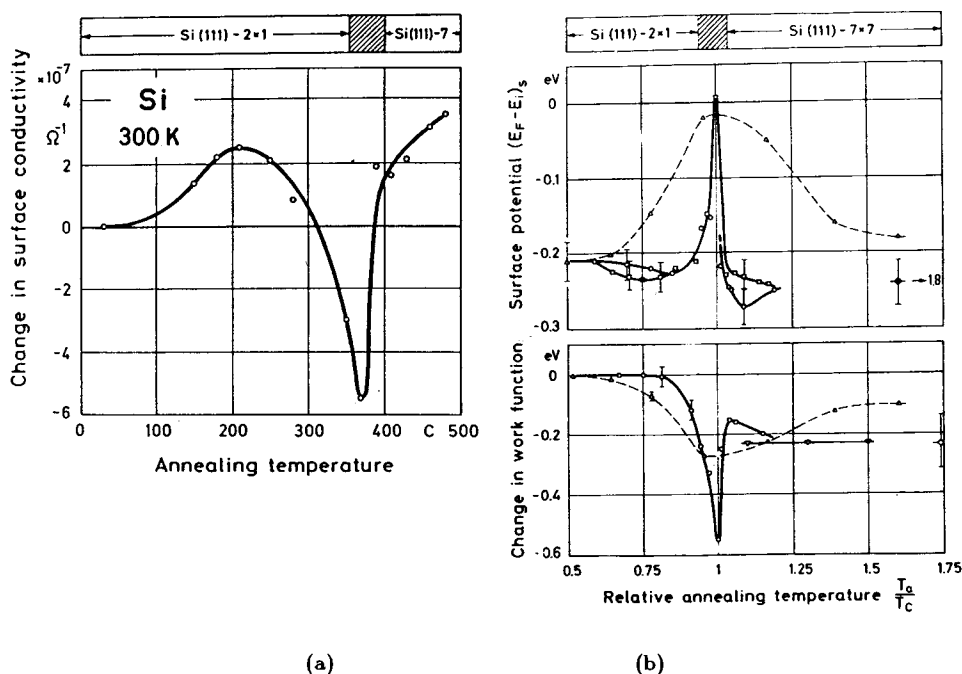
(a)   (b)

Fig. 9. (a) Changes in surface conductivity and LEED pattern of a cleaved Si(111) surface as measured at 300 K after isochronal annealing vs. annealing temperature.[62] The hatched area indicates the temperature range in which an apparent 1 × 1 structure is observed. (b) Changes in surface potential and work function during the same procedure.[63] The conversion temperature is $T_c = 630$ K.

3. Ag/Si(111)

3.1. *Atomic and electronic structures*

3.1.1. *Ag-induced surface structures*

The origin for the metal-induced reconstruction is a charge transfer between metal adatoms and substrate atoms, resulting in significant changes in surface electronic structures. These lead to instability of the surface-phonon structure, which drives the surface reconstruction at high temperatures to attain a lower total surface energy.

When Ag of 1ML (monolayer) is deposited onto the Si(111)-7 × 7 surface with subsequent annealing above 250° C, or when the Ag is deposited on the Si(111)-7 × 7 substrate maintained above 250° C, the surface structure is converted into a $\sqrt{3} \times \sqrt{3}(R30°)$. Figure 10(a) shows a RHEED pattern from the Si(111)-$\sqrt{3} \times \sqrt{3}$-Ag surface, and Fig. 10(b) shows its reciprocal rods arrangement. Since the first report on this surface,[65] this structure has been considered as a prototypical, nonreactive metal-semiconductor system, and has been a focal subject of almost every surface-science technique: diffraction and scattering methods, spectroscopies, and microscopies. As a result, many structural models for the surface have been proposed. The reader will find the relevant references on this subject in Refs. 6, 66, 67. After a long controversy, a honeycomb-chained-trimer (HCT) model proposed by Takahashi *et al.*[5,6] is found to be consistent with most of reported experimental results and first-principle calculations.[68,69] Figure 10(c) gives an illustration of the model. The $\sqrt{3} \times \sqrt{3}$-unit contains three Ag atoms. So the number of valence electrons in the unit cell is even, three from Ag atoms and nine from dangling bonds of three Si atoms. This is consistent with the semiconducting character of this surface, contrasting with the metallic nature of the Si(111)-7 × 7 surface. Figure 11 shows (a) angle-resolved UPS spectra[70] and (b) inverse photoemission spectra[71] for the Si(111)-$\sqrt{3} \times \sqrt{3}$-Ag surface. There is a distinct energy gap around the Fermi level, i.e., a semiconducting surface, which is reproduced by first-principles calculations.[68,69]

Kono *et al.*[72] found core-level shifts in soft X-ray photoemission spectra from Si $2p$ level during the development of the $\sqrt{3} \times \sqrt{3}$-Ag phase. They concluded that the Fermi level at this surface shifts 0.48-0.50 eV downwards as compared with the clean 7 × 7 surface, indicating an E_F position very close to the top of the valence band maximum E_{VBM} (0.13 ∼ 0.15 eV above the E_{VBM}).The amount of the E_F shift measured by Uhrberg[73] is slightly different from the value of Kono's group; a shift of 0.42 eV downwards to be located 0.21 eV above the E_{VBM}. In either case, the bands are found to bend sufficiently upward to create a p-type inversion layer on an n-type Si bulk (Fig. 11(c)). This means that the $\sqrt{3} \times \sqrt{3}$-Ag layer is negatively charged.

When the surface is maintained around 600° C, the Ag atoms thermally desorb from the $\sqrt{3} \times \sqrt{3}$ phase, resulting in the surface being converted to a 3 × 1
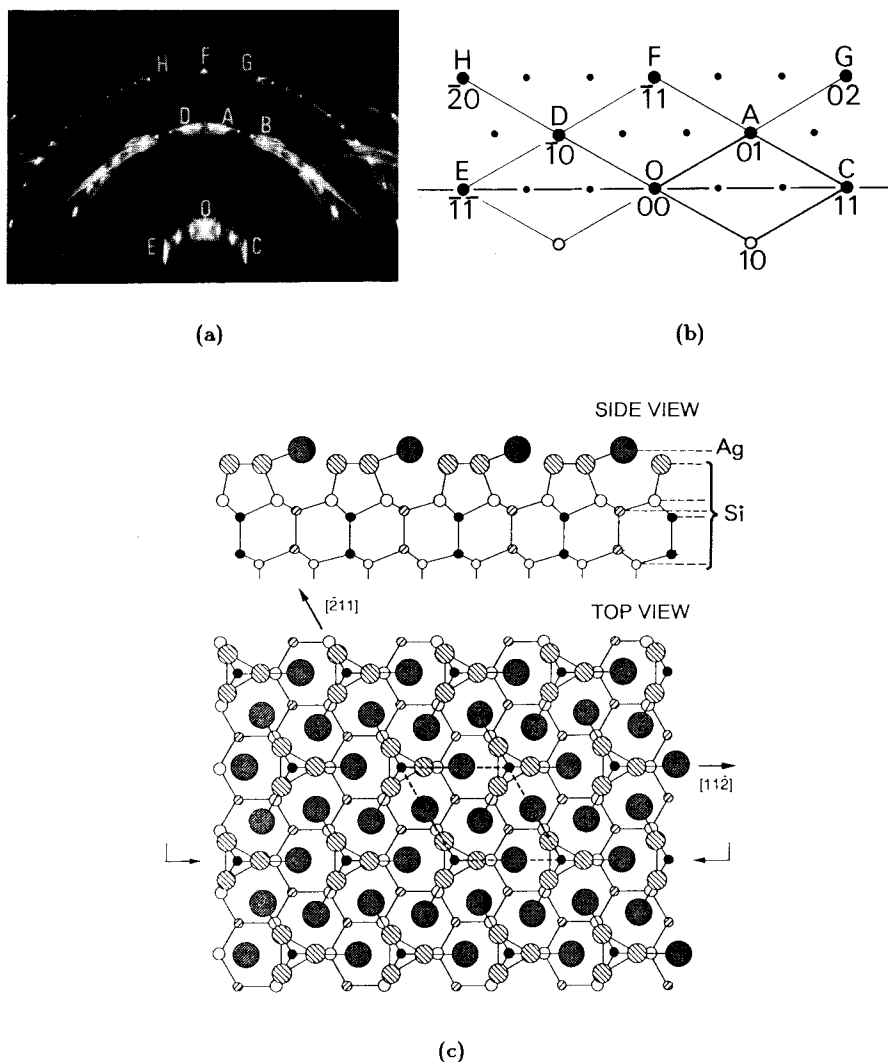
(a)

(b)

(c)

Fig. 10. Si(111)-$\sqrt{3} \times \sqrt{3}$-Ag structure. (a) Its RHEED pattern at room temperature in [11$\bar{2}$] electron incidence, (b) its two-dimensional reciprocal lattice, and (c) its honeycomb-chained-trimer (HCT) model proposed by Takahashi *et al.*[5,6]

structure. When this sample is cooled down to room temperature, 6×1 superlattice reflections emerge in the RHEED pattern and coexist with the 3×1 structure (Fig. 12).[74] Although the Ag-saturation coverage of this $(3 \times 1 + 6 \times 1)$ phase was measured to be 1/3 ML,[75-81] its detailed geometric arrangement of atoms is not yet clarified.[76,80-83]

(a)   (b)   (c)
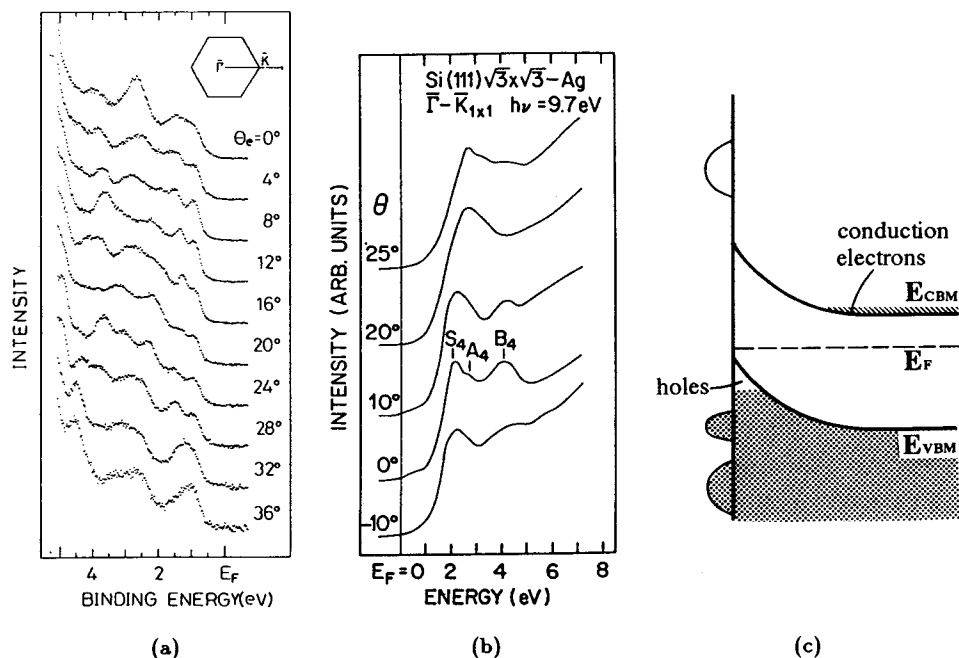
Fig. 11. (a) Angle-resolved UPS spectra as a function of polar angle θ_e for the Si(111)-$\sqrt{3} \times \sqrt{3}$-Ag surface.[70] (b) Angle-resolved inverse photoemission spectra from the same surface.[71] (c) Schematic illustration of band bending beneath the $\sqrt{3} \times \sqrt{3}$-Ag surface.
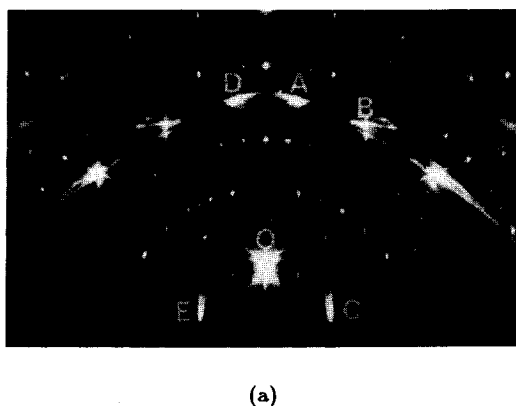

(a)

Fig. 12. RHEED pattern of (a) Si(111)-(3 × 1 + 6 × 1)-Ag surface at room temperature, and (b) its two-dimensional reciprocal lattice.

(b)
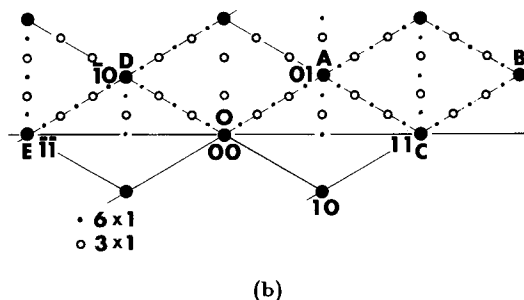
Fig. 12. (*Continued*)

3.1.2. *Ag growth at elevated temperatures*

When Ag atoms are slowly deposited onto the Si(111)-7 × 7 surface at elevated temperatures (250 ~ 500° C), the $\sqrt{3} \times \sqrt{3}$ superlattice reflections emerge and coexist with the 7 × 7 phase in the RHEED pattern, and gain in intensity with increasing Ag coverage. At 1 ML of Ag adsorption, the 7 × 7 spots disappear and only the $\sqrt{3} \times \sqrt{3}$ phase is observed as mentioned in the last section. With further Ag deposition, the RHEED pattern remains unchanged. This process is now understood to be a Stranski-Krastanov type growth (layer-plus-island growth).[84,85] Three-dimensional(3D) Ag micro-crystals nucleate after the completion of the $\sqrt{3} \times \sqrt{3}$ phase. This is because the surface energy is extremely lowered by the formation of the $\sqrt{3} \times \sqrt{3}$ structure compared with the 7 × 7 phase.[68] These indicate a drastic change in the Ag-binding mechanism with the substrate between before and after the completion of the $\sqrt{3} \times \sqrt{3}$ layer. Hence the deposited Ag atoms on top of the $\sqrt{3} \times \sqrt{3}$ layer have high mobility to nucleate into 3D islands of around 2μm in size,[74] of which number density is very small. This is the reason why the 3D Ag micro-crystals scarcely contribute to the RHEED pattern.

3.1.3. *Ag growth at room temperature*

If, after preparing the $\sqrt{3} \times \sqrt{3}$-Ag surface (Fig. 13(a)) at elevated temperatures and cooling it down to room temperature (RT), Ag of 4.5ML is deposited onto this surface, then RHEED patterns of Figs. 13(d)(d′) are observed. A transmission-type ring pattern from Ag micro-crystals, with spots in some preferential orientations, gradually emerges with deposition, while the $\sqrt{3} \times \sqrt{3}$ spots remain unchanged. This means that the deposited Ag atoms nucleate into 3D islands on the $\sqrt{3} \times \sqrt{3}$ phase and scarcely cover the substrate due to a high surface diffusivity of Ag adatoms. But since their diffusion length is relatively smaller compared with the case of high-temperature adsorption mentioned in the last subsection, where the 3D Ag nuclei are much smaller and its number density much higher. So the observable transmission-type diffraction spots from the 3D Ag micro-crystals emerge in the RHEED pattern.
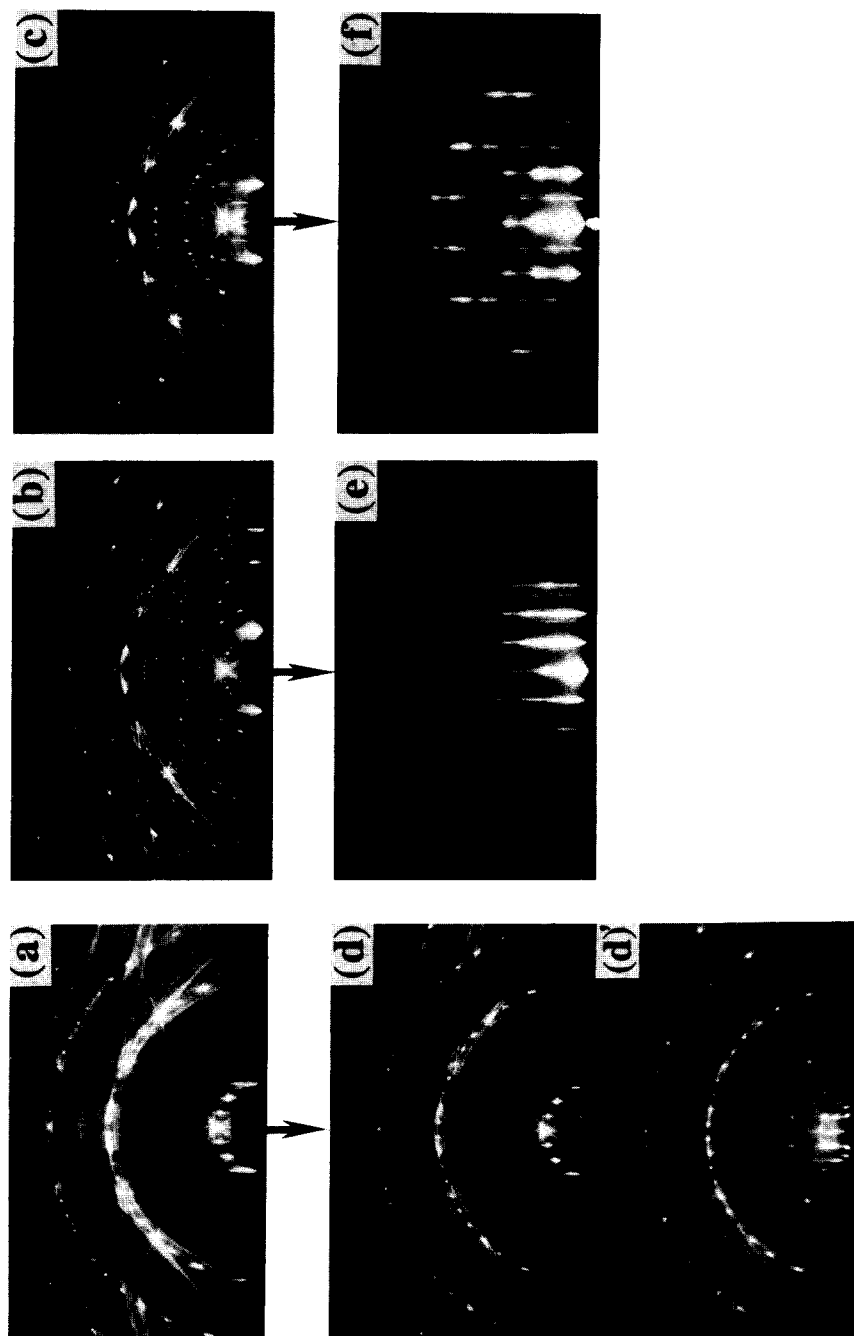
Fig. 13. RHEED patterns showing three different types of substrate surfaces, (a) Si(111)-$\sqrt{3} \times \sqrt{3}$-Ag, (b) clean Si(111)-7 × 7, and (c) Si(111)-(3 × 1 + 6 × 1)-Ag. After room-temperature deposition of 4.5 ML Ag onto each surface, the Ag grows in different ways (d) ~ (f). (d') is a small glancing-angle observation of (d).

Ag growth on the 7 × 7 surface (Fig. 13(b)) at RT is, on the other hand, quite different from that on the $\sqrt{3} \times \sqrt{3}$-Ag surface. As shown in Fig. 13(e), streaks (a reflection pattern) from Ag thin crystals appear in the RHEED pattern. This Ag layer is known to grow in quasi-layer-by-layer fashion (Frank-van der Merwe mode) up to a few ML, consisting of twining two-dimensional (2D) Ag thin crystals in a texture structure.[74,86] This [111] texture structure has preferential epitaxial orientation $[01\bar{1}]_{Ag}//[01\bar{1}]_{Si}$ on $(111)_{Ag}//(111)_{Si}$.

By closer observations by STM on the very early stage of Ag condensation onto a near-room-temperature 7 × 7 surface, the first Ag nuclei are found to be located on the inner adatoms of the 7 × 7-DAS unit cell, preferentially on the faulted halves.[87,88] Scanning tunneling spectroscopy (STS) results reveal the difference in electronic structures between at the Ag-covered and -uncovered areas on the surface. The dangling bonds of the clean 7 × 7 are saturated by Ag atoms, resulting in reduction of the local density of states at the Fermi level, converting into a semiconducting character, while the Ag-uncovered parts remain in a metallic character due to the dangling bonds of the DAS structure. The STM images[88,89] also shows deviations from an ideal layer-by-layer growth mode only at 3ML-Ag coverage.

In the case of room-temperature deposition of Ag onto the $(3 \times 1 + 6 \times 1)$ surface (Fig. 13(c)), the 6×1 superlattice reflections disappear around 0.2 ML coverage and only the 3×1 phase remains after that. With increasing Ag coverage, the structure is soon converted into 1×1, and the Ag layer grows in a similar style as in the case of the 7 × 7 substrate (Fig. 13(f)). But the rotations of the grown Ag thin crystals around the texture axis are more restricted, probably due to the influence of the underlying 3×1-structural atomic arrangement, and the Ag crystals are more 3D-like.

In addition to the Ag-induced surface structures and Ag-layer growth styles mentioned so far, another basic question concerning this Ag/Si(111) system is its interface structure after a thick Ag layer is deposited, which is a case of Schottky diode formation. Are the surface structures observed in monolayer Ag-coverage ranges preserved during thicker Ag layer growth? Recent grazing-incidence X-ray diffraction experiments[90] revealed that a 7 × 7 reconstruction of Si(111) surface is preserved under a room-temperature thick(260Å-thickness)-Ag deposition. This 7 × 7 periodicity is the remains of the DAS structure, presumably a stacking-fault layer. By depositing a thick Ag film onto the $\sqrt{3} \times \sqrt{3}$-Ag surface at RT, on the other hand, the $\sqrt{3} \times \sqrt{3}$ reconstruction is found to be suppressed, converted into a 1×1 structure. It is expected from this result that the Schottky barrier should be different between the two interfaces, Ag/Si(111)-7 × 7 and Ag/Si(111)-$\sqrt{3} \times \sqrt{3}$-Ag, because of the different interface atomic and electronic structures (see Sec. 3.2.2.).

3.2. *Electrical properties*

What is the correlation between the transport properties of Ag-covered Si(111) surface/interface and their microscopic structures such as geometric atomic arrange-

ments, electronic surface/interface states, Fermi-level shifts, and epitaxial-growth mechanisms ? It is, then, essentially important to simultaneously investigate both the structure and the electrical properties in UHV.

3.2.1. *Surface conductance and Hall effect*

In order to combine the measurements of surface conductance and Hall effect with simultaneous observations of RHEED in UHV during Ag growth, a special sample holder for a RHEED apparatus as shown in Fig. 14 was developed.[31] An *n*-type Si(111) wafer ($23 \times 5 \times 0.4 \, mm^3$ in size and resistivity of $48 \sim 50 \Omega$ cm) is mounted on a pair of Ta rods and clamped with Ta plates. Before each measurement run, various kinds of surfaces, clean 7×7, $\sqrt{3} \times \sqrt{3}$-Ag, and $(3 \times 1 + 6 \times 1)$-Ag, can be prepared by Ag deposition and direct heating by a current fed through the Ta-rod electrodes. The conductance of the central portion of the wafer under isothermal condition at RT was measured as a voltage drop between a pair of Ta wire contacts A and B, kept in elastic contact with the wafer, with a constant current of $10 \sim 100 \, \mu A$, supplied through the Ta rod electrodes. It took time from 30 min to 1 hour after the substrate-surface preparations at high temperatures to attain the isothermal condition at RT and for the resistance to be constant before measurement runs.
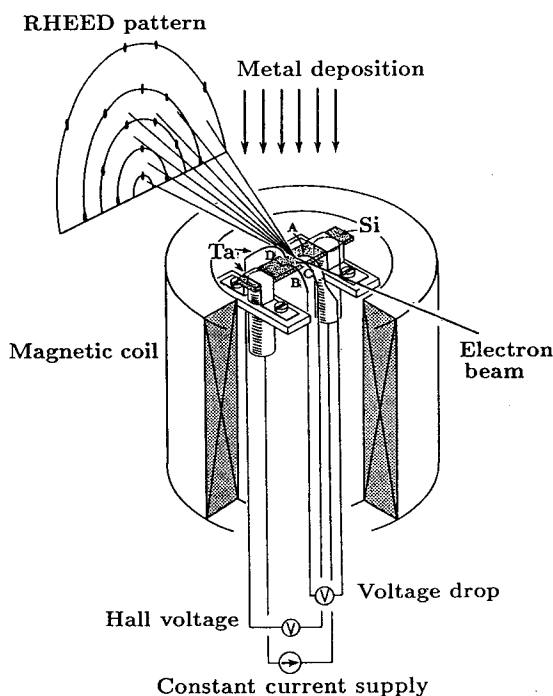

Fig. 14. The sample holder, drawn upside down, which enables simultaneous RHEED observations and electrical measurements during metal depositions in UHV.[31]

The Hall voltage was simultaneously measured through another pair of Ta wire contacts C and D which were set to be nearly perpendicular to the measuring current. The heat treatments for surface preparations with these Ta wires in contact make their contact resistances small and steady. A linear relation in the current-voltage characteristics was confirmed in the range from -1 to 1 mA with 0 V at 0 A. We carried out the same measurements mentioned below with Ta wire contacts on the backside of the Si wafer, instead of the front side contacts. The results were the same. So we can safely say that the changes in the voltage drops between the Ta wire contacts correctly correspond to the resistance changes, not to the changes of the contact potential difference caused by metal adsorption. Magnetic fields of ±340G, which were nearly perpendicular to the wafer surface, was applied with a coil composed of a ceramic-coating Al-Cu wire. Ag was evaporated at constant rates from alumina-coated W baskets which were placed about 50 cm away from the Si substrate. The amount of the deposited material, expressed here in units of ML (monolayer, 1 ML $= 7.8 \times 10^{14}$ atoms/cm^2), was monitored with a quartz-crystal oscillator. The structural changes of the surface area between the pairs of Ta wire contacts can be simultaneously analyzed with RHEED. Since the primary electron beam of about 1μ A in RHEED disturbed the voltages between the Ta wire contacts, the beam was always turned off during the measurement, except for the intermittent observations of the RHEED patterns in the course of Ag deposition. This holder enables azimuthal rotations, polar-angle tilts, and linear motions of the sample necessary for RHEED observations under proper conditions.

Figure 15(a) shows the change in resistance during Ag deposition (rate: 0.45 ML/min) onto the clean Si(111)-7 $\times$ 7 surface at RT.[29] The resistance is indicated as voltage drop between the Ta wire contacts. Changes in RHEED patterns in the course of deposition are also shown in the figure. The resistance does not show significant changes until the 7 $\times$ 7 pattern disappears around $2 \sim 3$ ML coverage, with the exception of a slight increase just after opening the evaporator shutter. In response to the subsequent development of a texture structure of the Ag film (Fig. 13(e)), the resistance begins to decrease steeply. With the deposition off, the resistance slightly raises.

In the case of Ag deposition onto the Si(111)-$\sqrt{3} \times \sqrt{3}$-Ag surface at RT, the growth style of the Ag film is quite different from that on the 7 $\times$ 7 surface as mentioned in Sec. 3.1.3., and accordingly the resistance also changes in a completely different way (Fig. 15(b)).[29] After an abrupt drop in the resistance at the beginning of deposition (less than 0.1 ML deposition), it decreases at a moderate rate during Ag deposition. As mentioned before, in this case, a ring pattern with some preferential-orientation spots from Ag micro-crystals gradually emerges in the RHEED pattern with increasing amount of deposition, while the clear $\sqrt{3} \times \sqrt{3}$ spots remain to the end. This is due to the high surface diffusivity of Ag adatoms on top of the $\sqrt{3} \times \sqrt{3}$ surface, enough to nucleate into 3D islands. An abrupt decrease in resistance at opening of the evaporator shutter and an abrupt increase at its closing suggest some influence of radiation from the Ag evaporator. However, radiation from the same
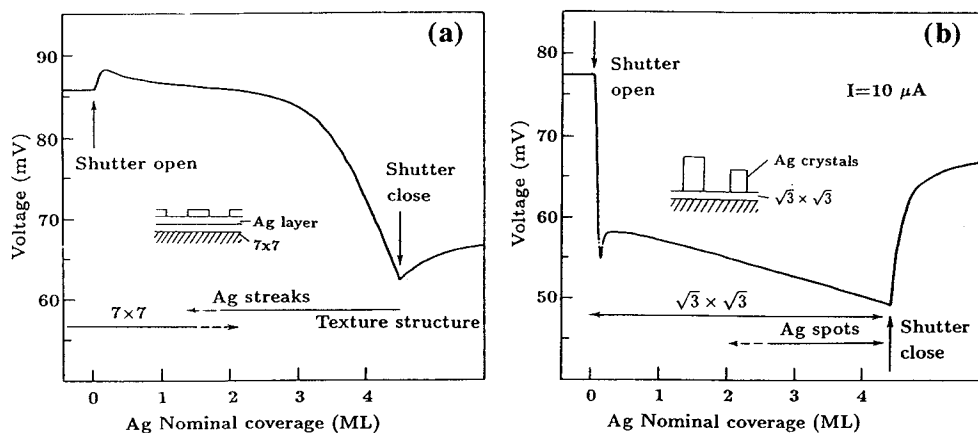
Fig. 15. Changes in resistance of a Si wafer and RHEED patterns during room-temperature Ag depositions onto (a) clean Si(111)-7 × 7 and (b) Si(111)-$\sqrt{3}$ × $\sqrt{3}$-Ag surfaces.[29]

type of empty evaporator, placed near the Ag evaporator and heated up to the same temperature, scarcely changed the resistance.[29] We can safely say, therefore, that it is the adsorbed Ag atoms that cause the resistance changes. Then, the steep rise in resistance after closing the evaporator shutter in Fig. 15(b) may correspond to a process of nucleation of Ag adatoms on the $\sqrt{3}$ surface as discussed below.

Figure 16(b) shows the change in the Hall voltage measured simultaneously with the resistance change shown in Fig. 16(a) by successively turning over the direction of the magnetic field (-340G and $+340$G alternately) without interruption of Ag deposition onto the clean Si(111)-7 × 7 surface at RT.[32] Because the pair of Ta-wire contacts C and D (Fig. 14) was not perfectly perpendicular to the measuring current, the voltage between the contact pair was not zero under zero-field but followed a similar change as the resistance change during Ag deposition. The zero level in Fig. 16(b) is obtained after subtracting the overall change under the zero field. The measured Hall voltage of 23μV at the 7 × 7 surface before Ag adsorption corresponds to a Hall coefficient R_H of -1.4×10^4 cm^3/coulomb which gives a carrier (electron) concentration of 4.6×10^{14} cm^{-3} from Eq. (12) assuming $r = 1$. The Hall voltage remains almost constant at the initial stage of deposition, during which the resistance also does not show any appreciable change. With the steep decrease in resistance by further deposition, the Hall voltage also begins to drop, signifying a steep increase in the carrier concentration.

Looking at the Hall voltage in Fig. 17(b) simultaneously measured with the resistance change shown in Fig. 17(a) for the Si(111)-$\sqrt{3}$ × $\sqrt{3}$-Ag surface during Ag adsorption at RT, in response to the steep drop in resistance at the beginning of deposition, the Hall voltage also abruptly decreases from 18 μV to 12 μV, and it remains small after that during the Ag deposition. This means an abrupt increase of the carrier concentration, from 5.9×10^{14} cm^{-3} ($R_H = -1.1 \times 10^4$ cm^3/coulomb) to
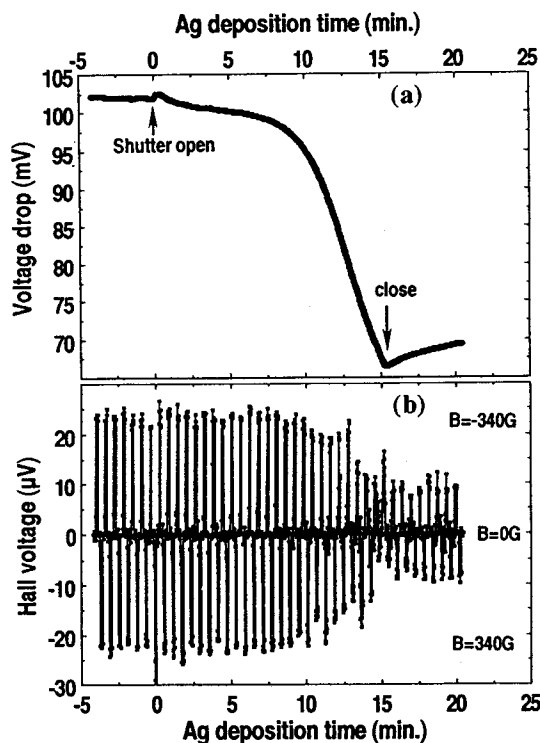
Fig. 16. Changes in (a) resistance and (b) Hall voltage of a Si(111) wafer with 7×7 surface at room temperature during Ag deposition.[32] The measuring current was 20 μA. The distances between Ta-wire contacts were different from those in the experiment of Fig. 15.

$8.9 \times 10^{14}\,\mathrm{cm}^{-3}$ ($R_{\mathrm{H}} = -7.1 \times 10^{3}\,\mathrm{cm}^{3}/\mathrm{coulomb}$) using Eq. (12). But these estimated values are not accurate because we should use Eq. (13) instead of Eq. (12) for an inhomogeneous semiconductor like the present case. In the case of an inversion layer at the surface space-charge region, the Hall coefficient for the layer has an opposite sign to that for the underlying bulk. But the measured Hall coefficient is dominant by the bulk contribution for the bulky sample (Eq. (13)). The increase in the Hall voltage, i.e., decrease in carrier concentration, after the evaporator shutter is closed correctly corresponds to the resistance rise shown in Fig. 17(a). Large deviations in the Hall voltage data points at opening and closing the evaporator shutter are artifacts originated from the inefficient data-processing program for subtracting the zero-level change under zero field.

In the case of deposition onto the $3 \times 1 + 6 \times 1$-Ag surface at RT (Fig. 13(c), (f)), surprisingly, the resistance scarcely changes during Ag deposition up to 5.6 ML coverage (Fig. 18).[30] The 6×1-RHEED pattern is quickly (around 0.2 ML) converted into 3×1 pattern after the Ag deposition starts, and then into 1×1 structure as mentioned in Sec. 3.1.3.
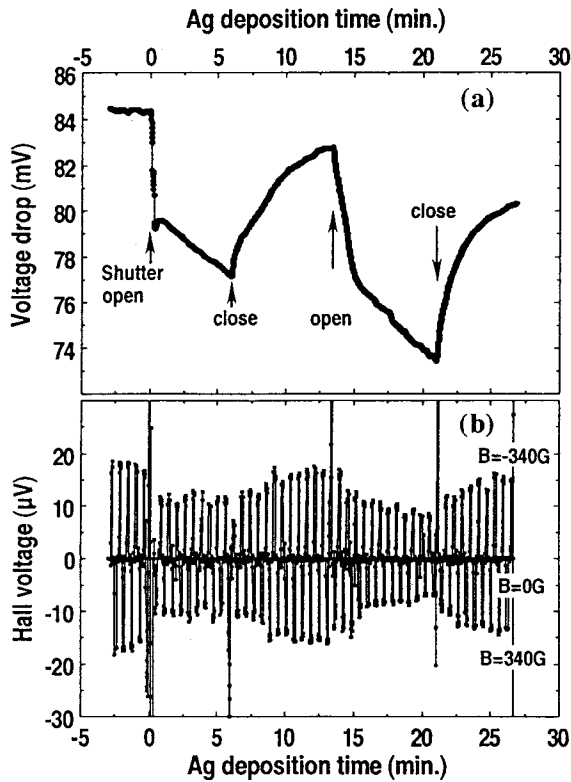
Fig. 17. Changes in (a) resistance and (b) Hall voltage of a Si(111) wafer with $\sqrt{3} \times \sqrt{3}$-Ag surface at room temperature during Ag deposition and its interruption.[32]
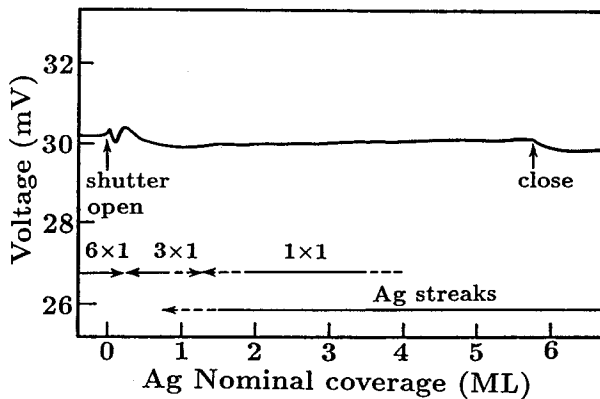

Fig. 18. Changes in resistance and RHEED patterns of a Si(111) wafer with $(3 \times 1 + 6 \times 1)$-Ag surface at room temperature during Ag deposition.[30] The distances between Ta-wire contacts were different from those in the experiments of Figs. 15, 16, and 17.

In this way, crucially depending on the substrate-surface structure, the epitaxial growth styles of room-temperature-deposited Ag layers as well as the surface-conductance and Hall-voltage changes are quite different.

During In deposition at RT, in place of Ag, onto the Si(111)-$\sqrt{3} \times \sqrt{3}$-Ag surface (Fig. 19), the resistance change is completely different from that shown in Fig. 15(b).[30] After a steep increase in resistance at the initial stage of In deposition, it remains almost constant in spite of the increase in In coverage. The $\sqrt{3} \times \sqrt{3}$-Ag structure is destroyed, to be converted into a 1 × 1 RHEED pattern at around 1.5-ML-In coverage. The Hall voltage changes in a consistent way with the resistance change in Fig. 20(b); the carrier concentration decreases at the initial stage of the deposition. This result should be distinctly contrasted with the case of Ag deposition onto the same $\sqrt{3} \times \sqrt{3}$-Ag surface in Figs. 15(b) and 17. The In adatoms on the $\sqrt{3}$-Ag surface seem to act electrically in a manner opposite to Ag adatoms.
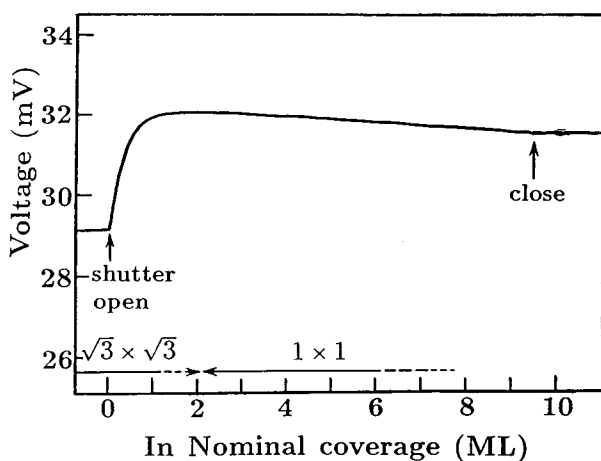

Fig. 19. Changes in resistance and RHEED patterns of a Si(111) wafer with $\sqrt{3} \times \sqrt{3}$-Ag surface at room temperature during In deposition.[30]

Figure 21 shows the photoemission spectra of the Si $2p$ core-level region (a) and the valence-band region for the Si(111)-7 × 7 surface covered with various amounts of Ag at RT (b).[91] The valence-band spectra (b) show that adsorption of only about 0.2 ML Ag causes a quick suppression of the dangling-bond state at the Fermi level (S_1 state), converting the surface into semiconducting from a metallic 7 × 7. This is consistent with the STS measurements by Tosch and Neddermeyer.[87,88] The core-level spectra (a) reveal an overall shift of the entire line shape to lower binding energies. This indicates an upward band bending of $\sim 0.26\,\mathrm{eV}$ by 1 ML Ag adsorption. In other words, the Fermi-level is depinned from the metallic S_1 state of the 7 × 7-DAS surface and the E_F position shifts from 0.63 eV down to
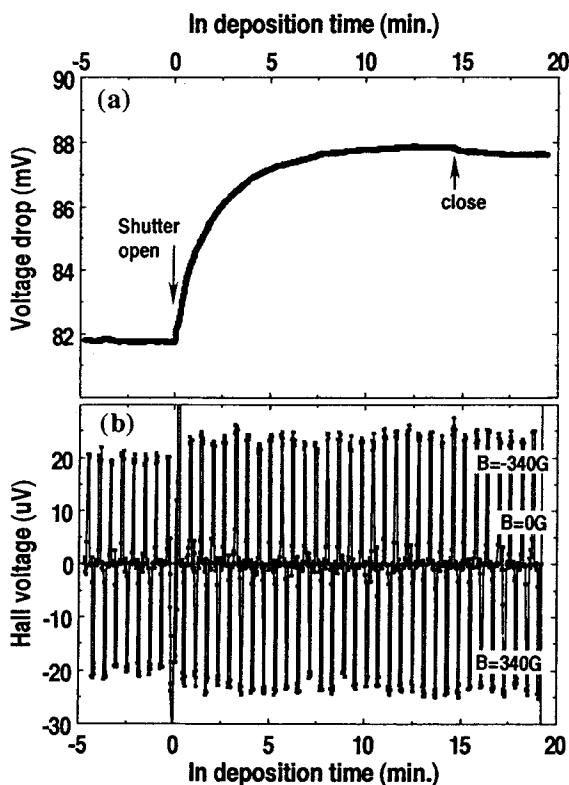
Fig. 20. Changes in (a) resistance and (b) Hall voltage of a Si(111) wafer with $\sqrt{3} \times \sqrt{3}$-Ag surface at room temperature during In deposition.[32]

0.37 eV above the valence-band maximum E_{VBM}. As shown in the calculated curve of the surface conductivity $\Delta\sigma$ versus the Fermi-level position (Fig. 8), the surface conductivity does not significantly change by this Fermi-level shift (from the point (c) to (e) in the figure). This is consistent with the measurement that the resistance shows no remarkable changes in the initial deposition of Ag (Fig. 15(a)).

A definite explanation for the observed slight increase in resistance at the very early stage of the deposition as shown in Fig. 15(a) is lacking at present. But, since this change corresponds to the saturation of the dangling-bond state as indicated in Fig. 21(b), the conversion from a "metallic" surface to a "semiconducting" one may cause such a resistance change. In other words, this may correspond to suppression of electron transport via the metallic surface state of the 7 × 7. The magnitude of this resistance change is not inconsistent with Henzler's estimation of conductivity via a metallic surface-state band.[28]
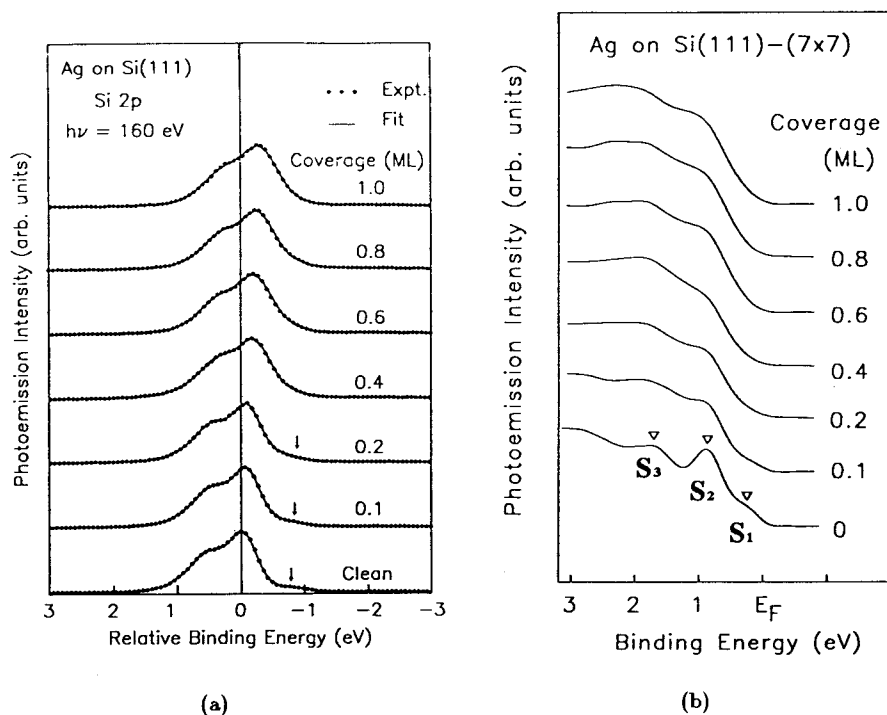
Fig. 21. X-ray photoemission spectra in (a) the Si 2p core-level region and (b) the valence-band region for Si(111)-7 × 7 surface covered with various amounts of Ag as indicated.[91]

Figure 22 shows the differential reflectivity spectra as a function of light energy taken from Si(111) surfaces with various amounts of Ag coverage.[92] The differential reflectivity $\Delta R/R$ is defined as

$$\frac{\Delta R}{R} = \frac{R^{\text{Si+Ag}} - R^{7\times7}}{R^{7\times7}} , \tag{15}$$

where $R^{7\times7}$ and $R^{\text{Si+Ag}}$ are the reflectivities of the clean Si(111)-7 × 7 surface and the Ag-adsorbed Si surface respectively. Figure 22(a) is for Ag deposition onto Si(111)-7 × 7 at near RT with coverages 0.1, 0.25, 0.49, and 0.70 ML (curves A to D). With increasing Ag coverage, the reflectivity of lower-energy light increases. This tendency is more clearly observed in Fig. 22(b) where the Ag coverage is higher, (A) 1.36 ML and (B) 2.47 ML. This means that Ag layer becomes metallic from semiconducting with coverage increase. This is because the initially adsorbed Ag atoms form covalent bondings with the dangling bonds of the Si substrate, resulting in a semiconducting character as indicated by the STS data[87,88] and UPS data (Fig. 21(b)), while, after the saturation of the Si dangling bonds, additional Ag atoms undergo metallic bonding among themselves. This process is accompanied by a delocalization of the "5s" valence electrons of the Ag atoms to become metallic. This must correspond to the steep decrease in resistance at 2 ∼ 3 ML Ag coverage
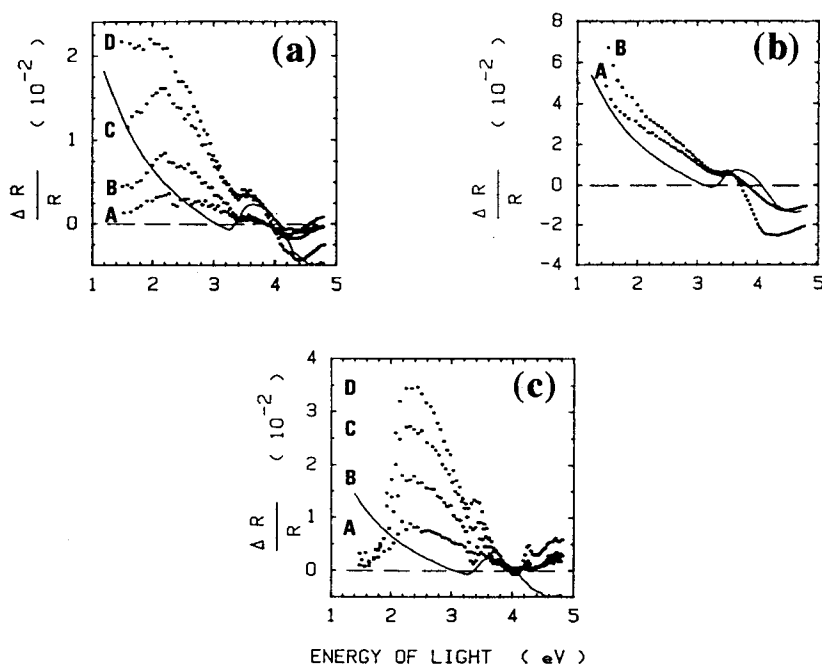
Fig. 22. Differential reflectivity spectra measured for various amounts of Ag deposited on Si(111) surfaces.[92] (a) Ag on the 7 × 7 phase at near room temperature for coverages 0.1, 0.25, 0.49, and 0.70 ML (A to D), (b) 1.36 (A), and 2.47 ML (B). (c) Ag on Si(111) at high temperature (with formation of the $\sqrt{3} \times \sqrt{3}$-Ag phase) for Ag coverage 0.18, 0.36, 0.52, and 0.69 ML (A to D). The continuous line is the calculated result for one layer of a free-electron metal.

in Fig. 15(a). Percolation paths of metallic conduction may be created around this coverage range. On the other hand, during development of Si(111)-$\sqrt{3} \times \sqrt{3}$-Ag (Fig. 22(c)), the semiconducting nature, lower reflectivity for lower-energy light, is preserved with the coverage increases.

With increase of the Ag coverage, the conduction through the grown metal film may dominate the resistance change, the effect of which strongly depends on the epitaxial growth mechanism. The rates of decrease in resistance during Ag deposition in the thicker coverage range (more than 3 ML) are quite different between Figs. 15(a) and 15(b). This seems to support the simple expectation that 2D Ag islands on the surface (a) more easily create percolation paths than 3D Ag nuclei (b).

Taking into account the fact that the Si(111)-$\sqrt{3} \times \sqrt{3}$-Ag surface is "semiconducting", the Fermi level at the surface is expected to shift easily with the subsequent Ag adsorption. Since the Fermi level is measured to lie at $0.1 \sim 0.2$ eV above the valence-band maximum (around the point (d) in Fig. 8) on the Si(111)-$\sqrt{3} \times \sqrt{3}$-Ag as mentioned before,[72,73] the steep drop in resistance at the beginning of the Ag deposition (Fig. 15(b)) must arise from a further downward shift of the E_{F} position

toward the valence-band maximum (i.e. further upward band bending), along the shift direction A from the point (d) in Fig. 8. This means that Ag atoms deposited on top of the $\sqrt{3} \times \sqrt{3}$-Ag layer act as acceptors, and introduce negatively charged acceptor-like surface states. A very small amount of Ag adatoms is enough to give rise to such a variation, resulting in an abrupt decrease in resistance at the beginning as shown in Fig. 15(b). But this change is recovered when the Ag deposition is stopped, leading to a steep increase in resistance. Figure 23(a) shows the resistance change during cycles of Ag deposition onto the Si(111)-$\sqrt{3} \times \sqrt{3}$-Ag surface at RT and its interruption. Steep decreases and increases in resistance are repeatedly observed at the opening and closing of the evaporator shutter, respectively. The recovering rise in resistance with the deposition off is considered to correspond to aggregation of the adsorbed Ag atoms in the $\sqrt{3} \times \sqrt{3}$ phase (Fig. 23(b)). This results in a decrease of charge transfer between the Ag adatoms and the substrate
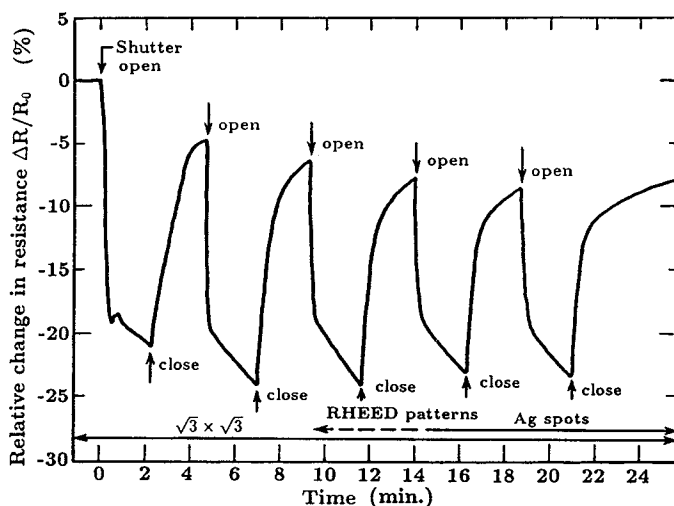
(a)
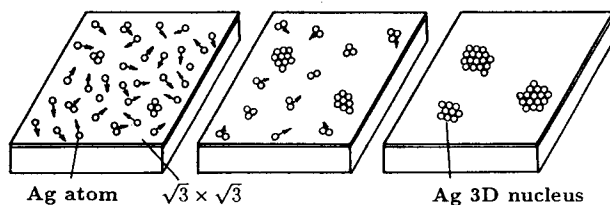
(b)

Fig. 23. (a) Resistance change during cycles of room-temperature Ag deposition onto Si(111)-$\sqrt{3} \times \sqrt{3}$-Ag surface and its interruption.[30] (b) Schematic illustration of the aggregation of adsorbed Ag monomers into three-dimensional Ag clusters on this surface.

to prevent further band bending. In other words, only isolated Ag atoms mainly give rise to the observed abrupt resistance drop. In order to observe this process by photoemission spectroscopies, the data must be collected without interruption of Ag deposition.

As the Fermi level position at the Si(111)-(3 × 1 + 6 × 1)-Ag surface has not yet been determined, a detailed discussion on the conductance measurements for this surface (Fig. 18) cannot be made. Two explanations for the lack of remarkable resistance change during Ag deposition are possible; E_F shift within the depletion region (Fig. 8) only or a strong E_F-level pinning effect. The onset of percolation conduction should be delayed compared with that of the Si(111)-7 × 7 surface due to the growth of more 3D-like Ag islands.

For the In deposition onto the Si(111)-$\sqrt{3} \times \sqrt{3}$-Ag surface (Figs. 19 and 20), the initial increase in resistance may be understood by the upward Fermi-level shift, along the direction B from the point (d) in Fig. 8. The In adatoms are considered to introduce donor-like surface states to reduce the negative charge in the $\sqrt{3} \times \sqrt{3}$-Ag layer. This E_F shift is opposite to that for the case of Ag adsorption on top of the same surface. In the region of thicker In coverages in Fig. 19, the metallic In layer does not seem to be conductive, probably because of 3D nucleation of In islands.

Thus the observed differences in resistance changes depending on the substrate-surface structures are understood with the aid of the data on the microscopic atomic and electronic structures.

3.2.2. *Schottky barrier*

Weitering *et al.*[25] measured the Schottky barrier heights (SBH) of Ag/Si(111) contacts with two types of interface structures, Ag/Si(111)-7 × 7 and Ag/Si(111)-$\sqrt{3} \times \sqrt{3}$-Ag. The former interface was prepared with RT deposition of Ag (0.1 μm thickness) onto the clean Si(111)-7 × 7 surface, while for the latter interface, an Ag layer of the same thickness was deposited at RT onto the Si(111)-$\sqrt{3} \times \sqrt{3}$-Ag surface. The growth styles of Ag layers and their interface structures for the two contacts are fairly different as mentioned in Sec. 3.1.3. The SBHs were determined by I-V measurements and curve fittings to the thermionic emission theory. Figure 24 shows a distribution of the measured SBHs on *n*-type Si wafers. The SBHs for the 7 × 7 interface cluster around 0.75 eV for both dopant ranges, lightly-doped ($3 \sim 6 \times 10^{14}$ cm^{-3}) and heavily-doped ($0.4 \sim 2 \times 10^{17}$ cm^{-3}) wafers, while for the $\sqrt{3} \times \sqrt{3}$ interface, the SBHs are different depending on the substrate dopant concentrations. Since, ideally, the SBH should be independent of the doping level of the semiconductor, this experimental result means nonuniformity of the SBH across the interface.[93] In *I–V* experiments, the diode current may preferentially flow through lower-barrier patches at the inhomogeneous interface, which are, however, effectively screened by the surrounding higher-barrier regions. Because the Debye screening length in semiconductors increases with decreasing dopant concentration, it is expected that the lowest SBHs are more effectively "masked" in lightly doped Si's.
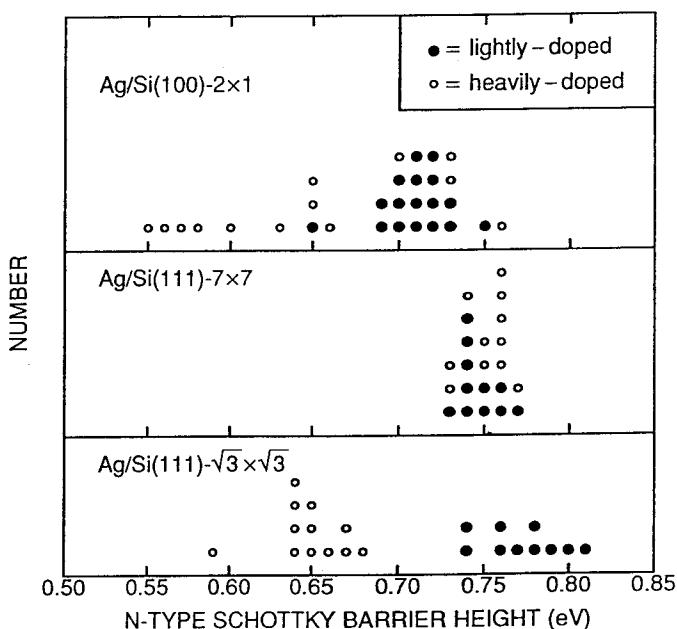
Fig. 24. Distribution of measured Schottky-barrier heights of Ag-*n*-type Si contacts prepared on Si(100)-2 × 1, Si(111)-7 × 7, and Si(111)-√3 × √3-Ag surfaces.[25]

Hence the difference in measured SBH for heavily-doped samples between the 7 × 7 and $\sqrt{3} \times \sqrt{3}$ interfaces lead to the conclusion that the SBH for the former interface is higher ($\sim 0.1\,\text{V}$) than that of the latter interface. The electrical inhomogeneity comes from structural inhomogeneity at the interface, because the Ag epitaxy on both substrates are far from perfect, especially for Ag/Si(111)-$\sqrt{3} \times \sqrt{3}$-Ag interface, as mentioned in Sec. 3.1.3.

As mentioned in Sec. 3.1.3., the atomic structures of the two interfaces are different in the presence or absence of the stacking-fault layer of the DAS structure at the outermost Si substrate near the interface. This may cause the difference of the Fermi-level-pinning position and the SBHs. The Schottky-Mott rule in which the SBH is determined only by the bulk parameters of the contact pairs (work function and electron affinity (Fig. 4(a))) does not work in this case, nor is the E_F-pinning level at the interface determined by the surface states of the semiconductor before contact (Fig. 4(b)). Since, as indicated in Fig. 21(b), the dangling bond states of the 7 × 7 structure are quickly suppressed by only submonolayer Ag adsorption, the interface states created during the contact formation work as a E_F-pinning level. The E_F is located at $0.37\,\text{eV}$ above E_{VBM} in this case. In the case of the $\sqrt{3} \times \sqrt{3}$-Ag surface, on the other hand, the superlattice is destroyed by deposition of thick Ag layer on it.[90] So its interface states is totally different from the surface states of the "bare" $\sqrt{3} \times \sqrt{3}$-Ag surface. The E_F position in this case is $0.47\,\text{eV}$ above E_{VBM}.

4. Au/Si(111)

4.1. *Atomic and electronic structures*

As in the case of Ag, Au deposition onto the Si(111)-7 × 7 surface with subsequent annealing induces several superlattice surface structures depending on its coverage: 5 × 2 (or 5 × 1), $\sqrt{3} \times \sqrt{3}$, and 6 × 6 structures. In spite of numerous investigations on this Au/Si(111) system, its nature is less clearly understood compared with the Ag/Si(111) system. No generally accepted atomic structural models for the superstructures exist at present. Even the saturation coverage for each structure has not yet been confirmed. This may be because Au has higher reactivity with Si than Ag, and they interdiffuse with each other near the surface, although Au and Si are known to form no thermodynamically stable bulk compound.[94-96] According to Molodtsov *et al.*,[96] like Ag, Au atoms have completely filled *d*-levels, which, however, are located closer to the Fermi level than in Ag. In Au/Si(111) system, the *d*-levels shift above E_F with increasing Au concentration due to *d/sp* hybridization. This mechanism makes Au resembled to the other *d*-transition metals, which are characterized by unfilled *d*-states and are highly reactive with Si.

Figure 25 shows phase diagrams of superlattice-surface structures for this system determined by (a) RHEED,[97,98] (b) LEED,[76] and (c) TED.[99] (d) shows intensities
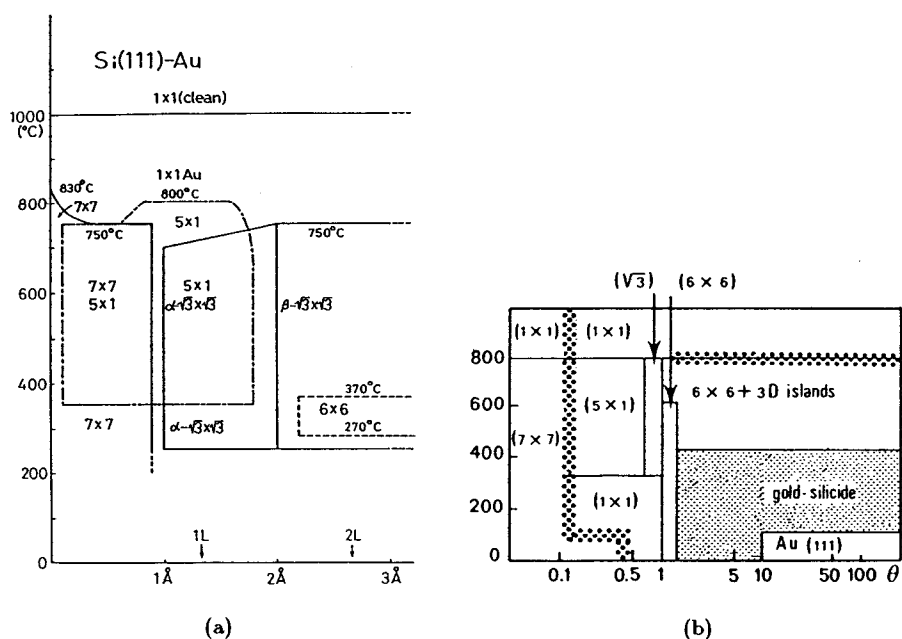

Fig. 25. Phase diagrams of Au/Si(111) system determined with (a) RHEED by Ino,[97,98] (b) LEED by LeLay,[76] and (c) TED by Takahashi *et al.*[99] (d) Intensities of Au 4*f* and Si 2*s* X-ray photoemission lines and evolution of LEED patterns as a function of Au coverage after high-temperature annealing.[100] The notation and saturate coverage for each structure are not consistent between the investigators. Note that the $\sqrt{3} \times \sqrt{3}$ phase seems to be complicated.
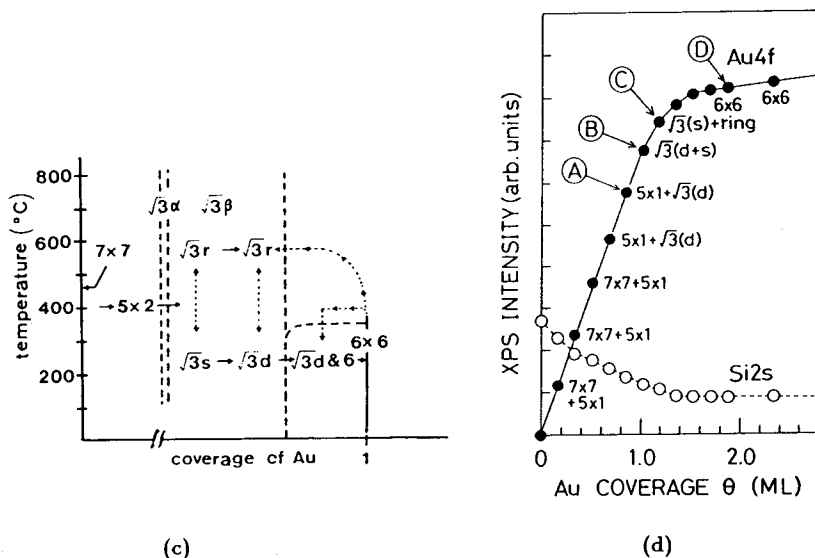
(c)

(d)

Fig. 25. (*Continued*)

of Au 4f and Si 2s X-ray photoemission lines and evolution of LEED patterns as a function of Au coverage.[100] After the completion of a 5 × 2 (or a 5 × 1) phase around 0.5 ML coverage, $\sqrt{3} \times \sqrt{3}$ and 6 × 6 phases develop with further Au adsorptions. The $\sqrt{3}$ phases are somewhat complicated as mentioned below.

Figure 26(a) and (b) show RHEED patterns at RT from the 5 × 2 structure around 0.5 ML-Au coverage, (c) is its two-dimensional reciprocal lattice, and (d) a schematic illustration of the superlattice unit cell and domains in real space. This consists of superlattice spots of a five-unit-cell periodicity along $\langle 11\bar{2} \rangle$ directions and streaks running between them, with three overlapping equivalent domains (a). These streaks indicate that a two-unit-cell periodicity along $\langle \bar{1}10 \rangle$ directions does not correlate with each other, although the five-unit-cell periodicity along $\langle 11\bar{2} \rangle$ directions are rigid. STM images[101] reveal rows oriented along $\langle \bar{1}10 \rangle$ directions with a five-unit-cell separation. Each row has an asymmetric structure with a two-unit-cell-periodicity which is not correlated between rows. The streaks in the RHEED pattern comes from this lack of long-range ordering of two-times periodicity.[102,103] This is due to stronger adsorbate-substrate interactions compared with adsorbate-adsorbate interactions.[104]

Figure 27(a) shows a RHEED pattern at RT of an "α-$\sqrt{3} \times \sqrt{3}$" structure around 0.7 ML-Au coverage. Its streaky superlattice reflections mean small coherent domains of the $\sqrt{3} \times \sqrt{3}$ phase. When the temperature is raised gradually, sharp spots emerge in the center of the streaky $\sqrt{3} \times \sqrt{3}$ reflections, gaining intensity with increasing temperature, at the cost of the intensity of the streaky reflections. Finally, around 500° C, the $\sqrt{3} \times \sqrt{3}$ reflections completely become sharp spots, as shown in the inset (a′). This apparently means a domain growth with increasing
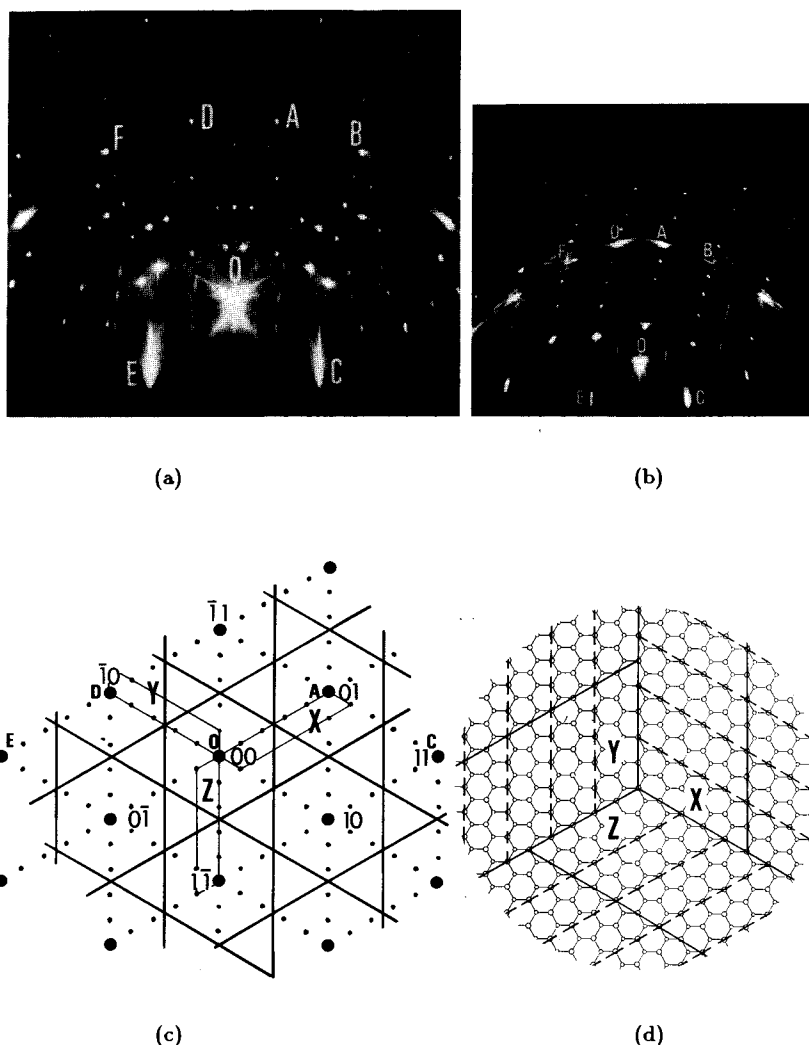
(a)   (b)

(c)   (d)

Fig. 26. (a) A RHEED pattern showing Si(111)-5 × 2-Au structure with three domains, and (b) that of single-domain surface. (c) Two-dimensional reciprocal lattice, and (d) its real-space illustration of three equivalent domains.

temperature. But the spots reversibly go back to the streaks by cooling down to RT. This indicates that larger $\sqrt{3} \times \sqrt{3}$-domains at high temperatures is broken up into smaller incoherent domains in the course of cooling. This reversible change with temperature could not be understood in terms of a simple domain growth and decay of a single type of $\sqrt{3} \times \sqrt{3}$ phase, rather the phenomenon suggests that the $\sqrt{3}$ phases at near RT and at higher temperatures are different in structure, and a kind of structural phase transition between them occurs with temperature change.
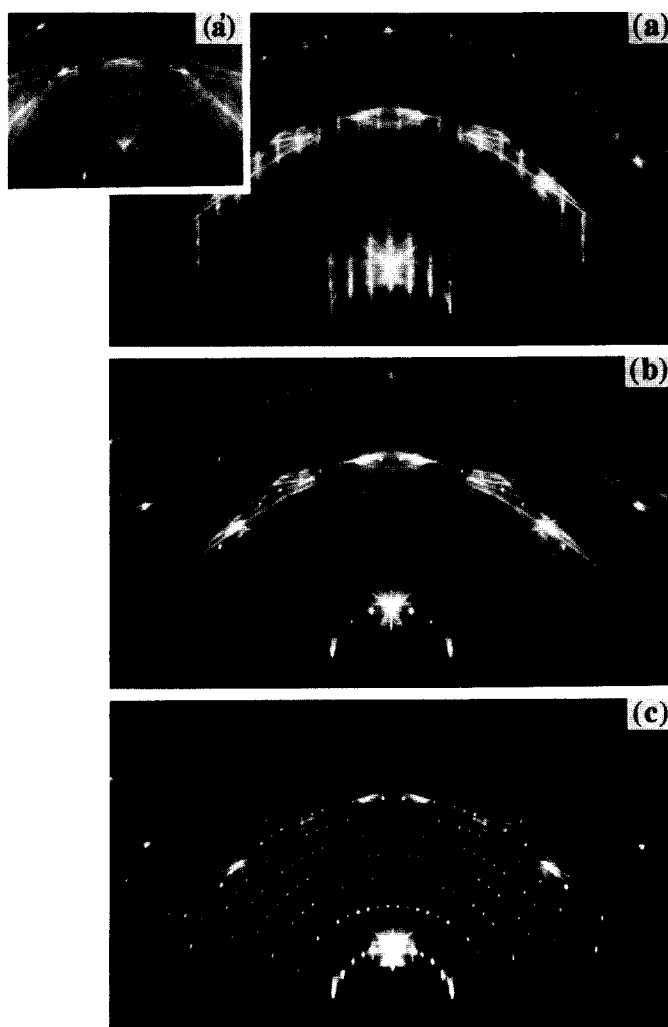
Fig. 27. RHEED patterns showing (a) Si(111)-α-$\sqrt{3}\times\sqrt{3}$-Au, (b)-β-$\sqrt{3}\times\sqrt{3}$-Au, and (c) -6 × 6-Au structures at room temperature. The streaky reflections of the α-$\sqrt{3} \times \sqrt{3}$-Au phase reversibly change into sharp superspots around 500° C as shown in the inserted pattern (a').

Figure 27(b) shows a RHEED pattern at RT from a "β-$\sqrt{3} \times \sqrt{3}$" structure around 1 ML-Au coverage, which has sharp superlattice spots with faint compli-cated streaks of irregular periodicity. These sharp spots remain unchanged when temperature increases. So this $\sqrt{3} \times \sqrt{3}$ phase should be distinguished from the α-$\sqrt{3} \times \sqrt{3}$ phase at a smaller coverage mentioned above. STM images[105,106] shows a centered hexagonal array of bright dots in the $\sqrt{3} \times \sqrt{3}$ phase and out-of-phase domain boundaries. Only a single bright dot is observed in the $\sqrt{3} \times \sqrt{3}$ unit cell, in contrast with the two bright dots in the unit cell of the Si(111)-$\sqrt{3} \times \sqrt{3}$-Ag.

Nogami *et al.*[106] found that the average spacing of the domain walls decreased with increasing Au coverage, i.e., the $\sqrt{3} \times \sqrt{3}$ phase was broken up into sub-100 Å size domains that decreased in size with increasing Au coverage. The 6×6 phase was suggested to be a periodic arrangement of small $\sqrt{3} \times \sqrt{3}$ domains.

The 6×6 phase with Au coverage of more than 1 ML (Fig. 27(c)) can be built up by annealing at around 300° C. The 6×6-RHEED pattern has an especially high background, meaning a randomness in structure. The correlation with these STM[106] and our RHEED observations is not clear at present.

Figure 28 shows the normal emission spectra of ultra-violet photoemission spectroscopy from Si(111)-7 × 7-clean, -5 × 2-Au, -α-$\sqrt{3} \times \sqrt{3}$-Au, -β-$\sqrt{3} \times \sqrt{3}$-Au, and -6 × 6-Au surfaces, respectively, which were excited with He I radiation (21.2 eV).[107] The well-known surface states S_1 and S_2 of the clean 7 × 7 surface are indicated (see also Fig. 3(a)). At normal emission, a prominent peak B at 1.9 eV below the Fermi level E_F is known to correspond to the bulk feature, not to the third surface state S_3 in Fig. 3(a).[3,108] For the surfaces with Au-induced superstructures, this bulk
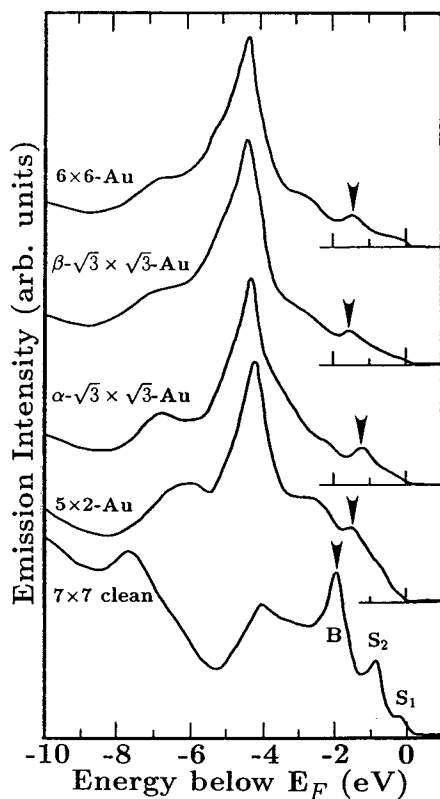

Fig. 28. Normal-emission UPS spectra taken from Si(111)-7 × 7 clean surface and Si(111) surfaces with Au-induced superstructures (reproduced from Ref. 107).

peak survives as small peaks indicated by arrow heads, of which the positions are observed to shift toward E_F as compared with the 7×7 surface; shifts of 0.45-0.6 eV. This signifies upward band bendings at the surfaces. Because the Fermi level E_F of the clean 7×7 surface is pinned at 0.63 eV above the valence-band maximum E_{VBM} as mentioned in Sec. 2.1, the E_F at the Au-induced superstructure surfaces is then located around 0-0.2 eV above E_{VBM}. The E_F at the $\sqrt{3} \times \sqrt{3}$-Au surface was also determined using Si $2p$ core-level photoemission spectroscopy to be 0.33 eV above E_{VBM}.[109] The upward band bending is almost enough to create a p-type inversion layer in the surface space-charge region on an n-type bulk Si, as in the case of the Si(111)-$\sqrt{3} \times \sqrt{3}$-Ag surface (see Sec. 3.1.1.).

Figure 29 shows a series of RHEED patterns during Au adsorption onto the Si(111)-7×7 at RT. With increase of Au coverage, the 7×7-superlattice spots gradually blur up to around 1 ML (a)–(c). But at about 1.5 ML coverage, the superspots temporarily regain their intensities as shown in (d), of which the relative intensity ratios are different from those of the clean 7×7 (a). For instance, the ($\frac{3}{7}$, $\frac{3}{7}$)-order spot on the 0th Laue zone in (a) is the most intense, which originates from the adatom array with 2×2 periodicity in the DAS structure (see Sec. 2.1). This fractional-order spot is, on the other hand, the weakest in (d), signifying a partial structural change in the 7×7 unit. Over 2 ML coverage, diffraction spots, even the fundamental spots, are hardly observed only a diffuse background remaining. This means an amorphous-like surface layer with Au-Si mixture.
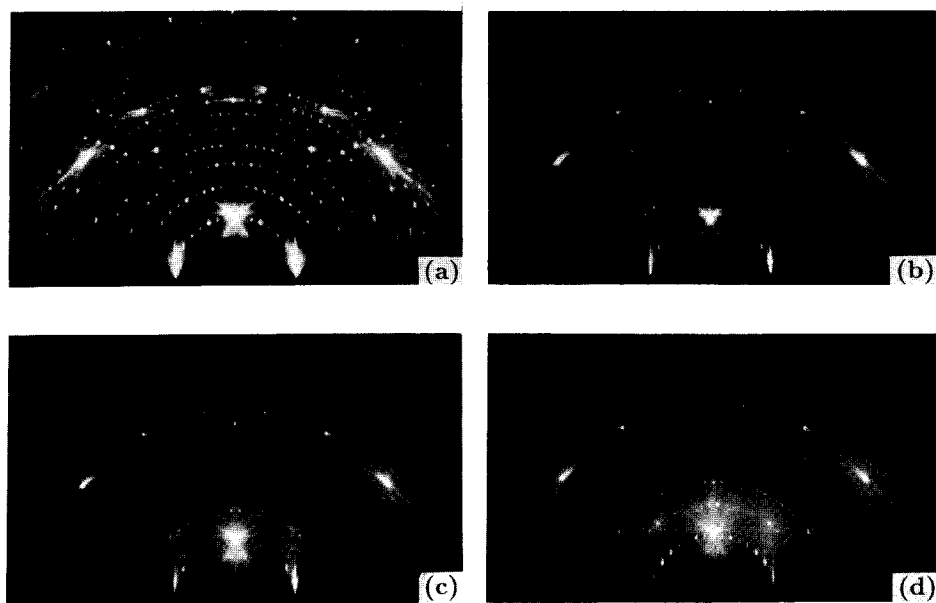

Fig. 29. A series of RHEED patterns during Au deposition onto clean Si(111)-7 × 7 surface at RT. Au coverages are (a) 0, (b) 0.6, (c) 1, (d) 1.5, (e) 1.8, and (f) 2.1 ML. Notice the change in relative intensity ratios between the superlattice spots during blurring out.
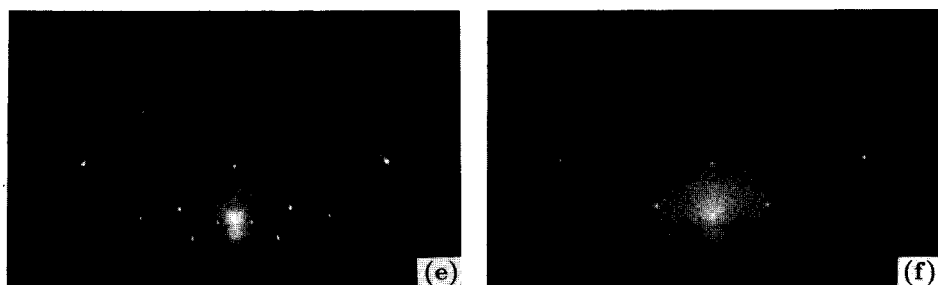
Fig. 29. (*Continued*)

Molodtsov *et al.* observed energy shifts of Si $2p$ core level to lower binding energies with Au adsorption onto the Si(111)-7 × 7 surface at RT.[96] This Au-induced energy shifts caused by upward band bending reached a maximum value of -0.43 eV at 2Å (1.6 ML) Au coverage. In other words, the Fermi level shifts from 0.63 eV to 0.20 eV above E_{VBM} with monolayer-range Au deposition.

## 4.2. *Electrical properies–surface conductance and Hall effect*

Figure 30 shows changes in resistance of the Si wafer during Au deposition (rate = 0.21 ML/min) onto (a) the clean Si(111)-7 × 7 and (b) the Si(111)-5 × 2-Au surfaces at RT, respectively.[29] Changes in RHEED patterns in the course of deposition are also shown in the figure. In (a) the resistance does not show a significant change at the initial deposition, except for a slight increase at the beginning, similar to the Ag case (Fig. 15(a)). The subsequent decrease in resistance temporarily slows down around 1.5 ML coverage, during which the 7 × 7 pattern seems different from that of the clean surface in the relative intensity ratios among the superlattice spots (Fig. 29(d)). After that, the pattern becomes 1 × 1 with increasing background intensity.

In contrast, a similar experiment with the Si(111)-5 × 2-Au surface reveals quite different changes in resistance as shown in Fig. 30(b). As soon as the Au deposition starts, the resistance shows steep increase, and reaches its maximum at Au coverage of 0.1 ∼ 0.2 ML. This range of coverage corresponds to a minor change in the RHEED pattern: the half-order streaks in the 5 × 2 pattern disappear to convert to a 5 × 1 structure. Passing through the maximum, the resistance begins to decrease, and the 5 × 1 structure is destroyed into a 1 × 1 pattern with more Au deposition.

The simultaneously measured Hall voltages with magnetic fields of ±340 G show consistent variations with the resistance changes as shown in Fig. 31(b) and 32(b).[32] In Fig. 31 the Hall voltage does not show any appreciable change at the initial stage of Au deposition onto the 7 × 7 surface, and gradually decreases with resistance drop at thicker coverage range. In the case of the 5 × 2-Au surface (Fig. 32), the Hall voltage rises from 18 μV to 23 μV at the beginning of the deposition and subsequently decreases. This shows the carrier density actually decreased temporarily with only
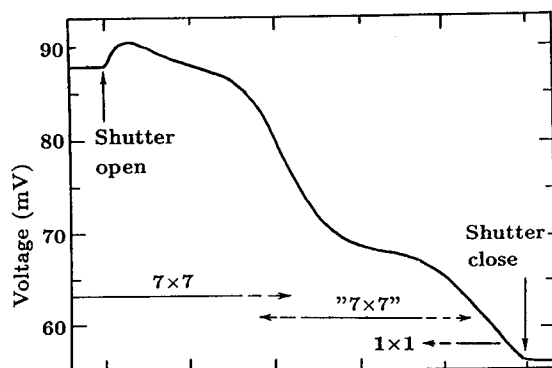
(a)
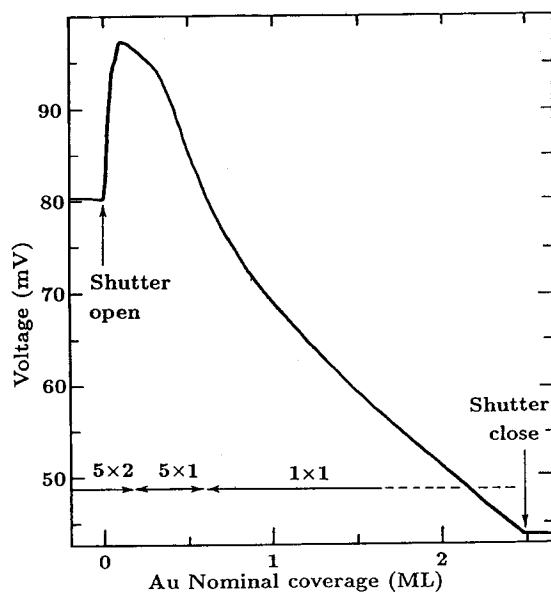
(b)

Fig. 30. Changes in resistance of the Si wafer and RHEED patterns during room-temperature Au depositions onto (a) clean Si(111)-7 × 7, (b) Si(111)-5 × 2-Au surfaces.[29]

0.1 ML Au deposition, from 5.9×10^{14} cm^{-3} ($R_H = -1.1 \times 10^4$ cm^3/coulomb) to 4.6×10^{14} cm^{-3} ($R_H = -1.4 \times 10^4$ cm^3/coulomb), as estimated by Eq. (12). But, as in the case of the $\sqrt{3} \times \sqrt{3}$-Ag surface in Sec. 3.2.1, these estimated values are not accurate because of the inhomogeneity due to band bending.
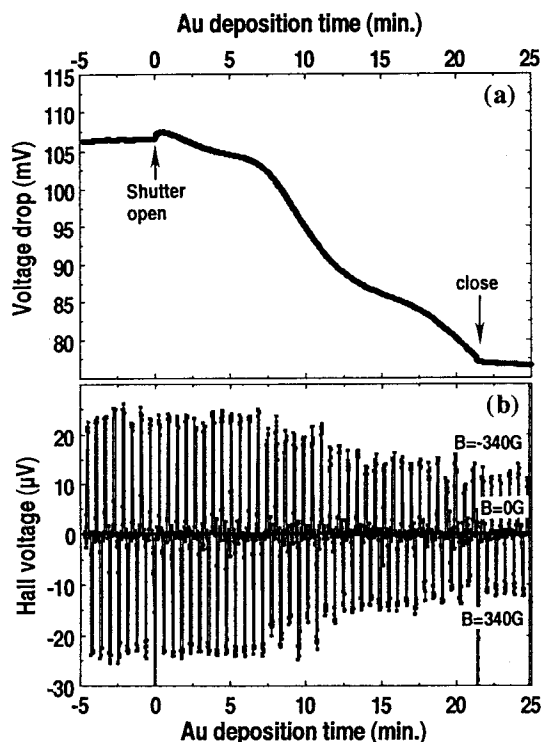
Fig. 31. Changes in (a) resistance and (b) Hall voltage of Si(111) wafer with 7 × 7 surface at room temperature during Au deposition.[32] The measuring current was 20 μA. The distances between Ta-wire contacts were different from those in the experiment of Fig. 30.

Similar changes in resistance and Hall voltage are observed for other Au-induced-superstructure substrates as shown in Fig. 33.[30] But the magnitudes of the initial increases in resistance are different depending on the initial surface structures; the resistance increases most greatly for the case of 6 × 6-Au surface, during which the RHEED pattern is converted into a $\sqrt{3} \times \sqrt{3}$. The final RHEED patterns with 2.8 ML Au deposition in all cases are almost the same faint 1 × 1 with high background intensity, irrespective of the different starting surface structures. The decrease rates of the resistance in thicker coverage ranges also do not depend on the initial surface structures. These results contrast to the Ag case in Fig. 15.

Figure 34 shows the resistance change during cycles of Au deposition onto the Si(111)-5×2-Au surface at RT and its interruption.[30] The resistance follows a similar change as shown in Fig. 30(b) during the deposition periods, but it remains constant during the interruption periods. This contrasts with the case of Ag deposition onto the Si(111)-$\sqrt{3} \times \sqrt{3}$-Ag surface (Fig. 23). This difference between Ag and Au cases is attributed to the difference in surface diffusion and nucleation of deposited adatoms. The difference in reactivity with Si can affect the phenomena too.
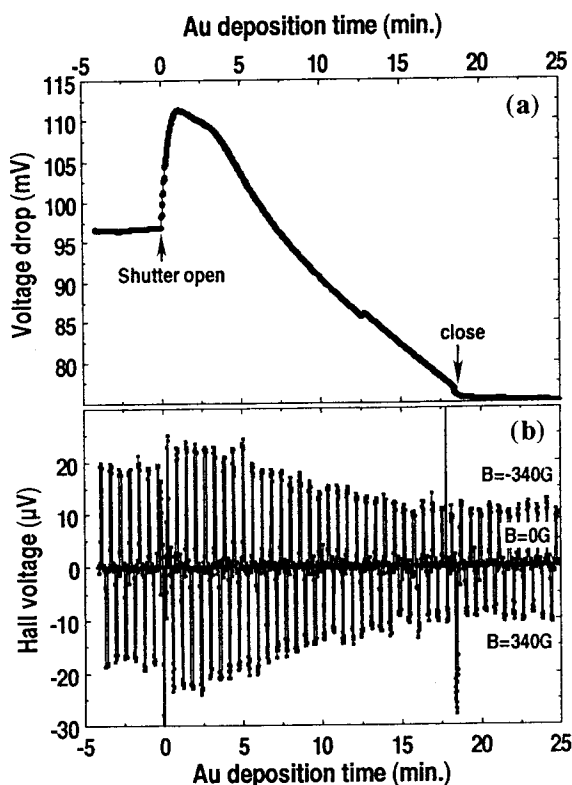
Au deposition time (min.)

Fig. 32. Changes in (a) resistance and (b) Hall voltage of a Si(111) wafer with Si(111)-5 × 2-Au surface at room temperature during Au deposition.[32]

Figure 35 shows the resistance change during Cs deposition onto the Si(111)-5 × 2-Au surface at RT.[31] In this case, again, the resistance largely raises at the beginning of deposition. Comparing with Fig. 30(b), it is suggested that the adatoms of Cs and Au on top of the 5 × 2-Au surface act electrically in a similar way.

As in the case of Ag/Si(111) in Sec. 3, the changes in resistance and Hall coefficient on the initial stages of Au depositions are understood in terms of the band bending and excess surface carriers. For Au deposition onto the Si(111)-7 × 7 surface, the data of photoemission spectroscopy[96] indicate then the E_F shift is restricted only in the depletion range in Fig. 8. This does not raise significant changes in resistance at the initial deposition shown in Fig. 30(a). The photoemission spectroscopies in Fig. 28 show that the E_F positions at the ordered Au-covered Si(111) surfaces are located close to the E_{VBM}, around the point (d) in Fig. 8, so that the surface space-charge layers are inversion ones. The remarkable increases in resistance just after the beginning of the depositions in Figs. 30(b) and 33(b)–(e) and the corresponding increase of the Hall voltage in Fig. 32(b) can be explained by the E_F shift in the direction B from the point (d) in Fig. 8. This fact means that

additional Au adatoms on the Au-induced-superstructure surfaces introduce donor-like surface states, resulting in a reduction of the negative chargetrapped in the surface states. This action is contrasted with the additional Ag adsorption on top
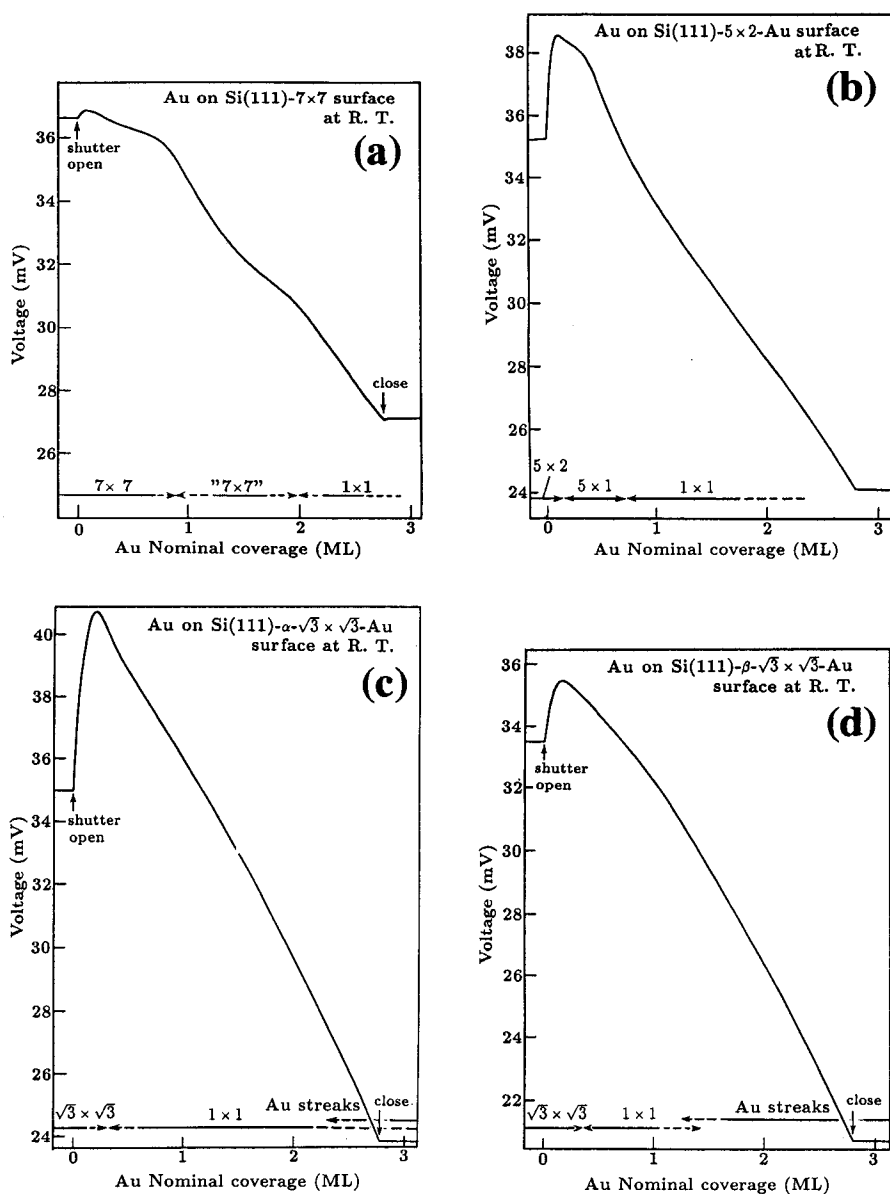

Fig. 33. Changes in resistance and RHEED patterns during the room-temperature Au depositions onto (a) clean Si(111)-7×7, (b) Si(111)-5×2-Au, (c) Si(111)-α-$\sqrt{3}$×$\sqrt{3}$-Au, (d) Si(111)-β-$\sqrt{3}$×$\sqrt{3}$-Au, and (e) Si(111)-6 × 6-Au surfaces.[30]
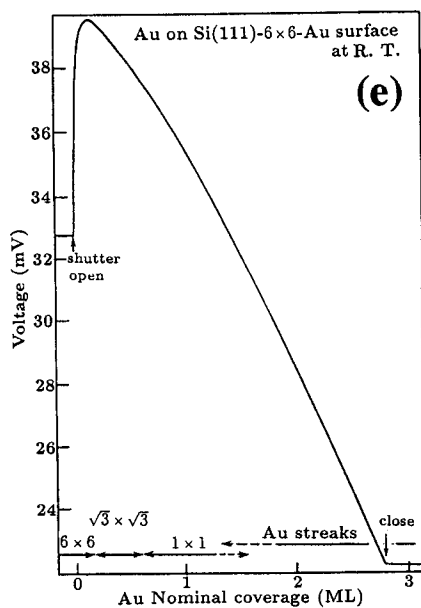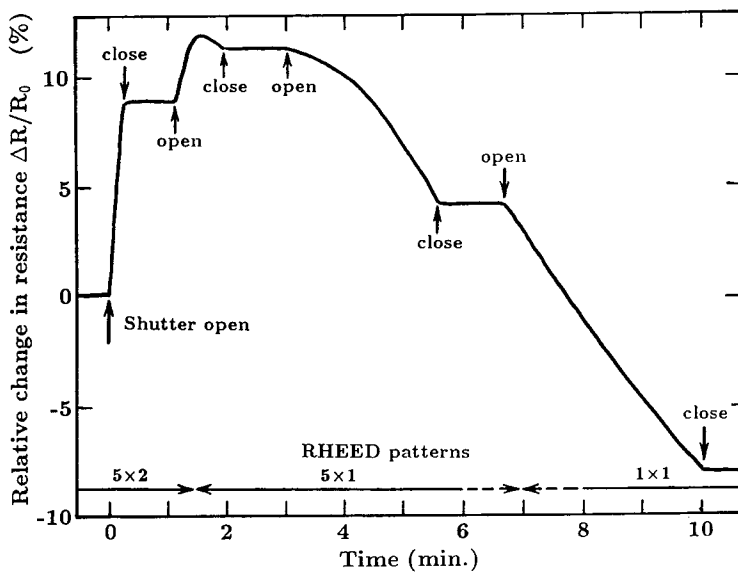
Fig. 33. (*Continued*)

Fig. 34. Resistance change during cycles of room-temperature Au deposition onto Si(111)-5 × 2-Au surface and its interruption.[30]
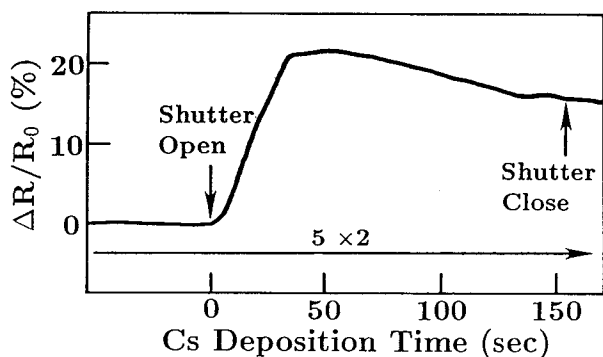
Fig. 35. Change in resistance and RHEED patterns of a Si wafer with Si(111)-5 × 2-Au surface during room-temperature Cs deposition.[31]

of the Si(111)-$\sqrt{3} \times \sqrt{3}$-Ag surface (Sec. 3) in which acceptor-like surface states are introduced to make the surface more negatively charged. Thus the charge transfers between the adsorbates and the substrates are opposite in the Ag and Au cases. This may be an interesting subject for theoretical calculations.

After reaching the maxima in resistance for the duration of Au depositions on the ordered Au-covered surfaces (Figs. 30(b) and 33(b)–(e)) the resistances begin to decrease. With an increase of the metal coverages, the donor- or acceptor-like actions of the additionally adsorbed atoms mentioned so far will change because of the mutual interactions between the adatoms. That is, the charge transfers between the adsorbates and the substrates will change with aggregation of isolated adatoms on the surface. So the above-mentioned simple picture of band bending and "surface doping" effect by adatoms will have to be modified near 1 ML coverage. Furthermore, since the RHEED patterns of the 5 × 2, $\sqrt{3} \times \sqrt{3}$'s, and 6 × 6 structures disappear to become 1 × 1 with less than 1 ML coverage, the surface electronic states can totally redistribute, and the E_F positions will not correlate with those at the initial surfaces.

Similar 1 × 1 RHEED patterns and similar decrease rates of the resistances in the Au coverage regions thicker than 1 ML for all the surfaces in Fig. 33 suggest that the resulting surface layers, probably mixtures of Au and Si, have similar structures, irrespective of the initial surfaces. This contrasts with the Ag (Sec. 3) and In (Sec. 5) cases in which the initial substrate-surface structures strongly affect the nature of the grown metal layers. This difference between Ag/In and Au may originate from the difference in reactivity with Si. These considerations will lead to the expectation that the Schottky barriers of Au-Si(111) contacts are not dependent on the substrate surface structures, as in the cases of Ag/Si (Fig. 24) and Pb/Si contacts.[22–24]

5. In/Si(111)

5.1. *Atomic and electronic structures*

5.1.1. *In-induced surface structures*

Since the first report by Lander and Morrison,[110] group-III metal(Al, In, or Ga)-adsorbed Si(111) surfaces have been investigated as frequently as the noble metal/Si(111) systems. Three kinds of superstructures are known to appear by In adsorption onto the Si(111)-7 × 7 surface with heat treatments. Figure 36(a) shows the phase diagram of the surface structures as functions of In coverage and substrate temperature.[111] RHEED patterns of the respective structures are also shown: (b) Si(111)-$\sqrt{3} \times \sqrt{3}$-In, (c) Si(111)-$\sqrt{31} \times \sqrt{31}$-In, and (d) Si(111)-4 × 1-In. Of these phases, the nature of the $\sqrt{3} \times \sqrt{3}$-In has been studied in greatest detail. The saturation coverage of In for this phase is determined to be 1/3 ML, i.e., one In adatom in the $\sqrt{3} \times \sqrt{3}$-unit mesh. Then, this trivalent atom can entirely satisfy all the dangling bonds on the Si(111) surface. Al or Ga induced $\sqrt{3} \times \sqrt{3}$ phase is also considered to be of the same structure. From a first-principles calculation of the total energy, Northrup[112] found two atomic sites for Al to be in the lowest energy states: threefold hollow site (H_3 model) and threefold on-top site of the second-layer Si atom (T_4 site). Since the both models lead to similar electronic states, angle-resolved photoemission spectroscopy[113,114] could not differentiate between them. STM observations revealed no evidence of co-adsorption
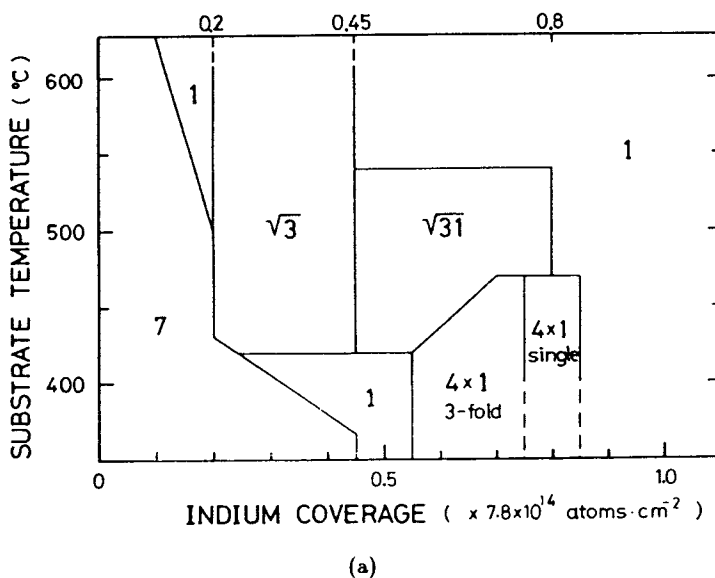

Fig. 36. (a) A phase diagram of In/Si(111) system determined by RHEED.[111] (b)–(d) RHEED patterns showing (b) Si(111)-$\sqrt{3} \times \sqrt{3}$-In, (c) Si(111)-$\sqrt{31} \times \sqrt{31}$-In, and (d) Si(111)-4 × 1-In phases. (e) T_4 structural model for the Si(111)-$\sqrt{3} \times \sqrt{3}$-In phase.
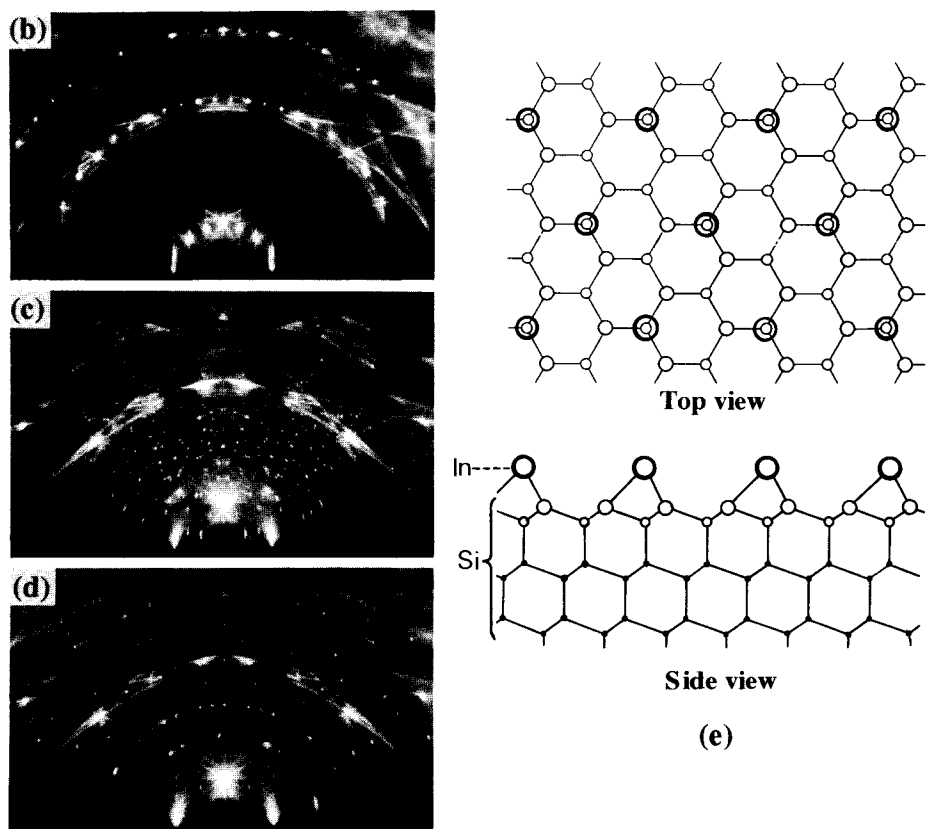
Fig. 36. (*Continued*)

on H_3 and T_4 sites on different areas of any single image.[115] Ion scattering spectroscopy experiments suggest a T_4 model for the $\sqrt{3}$-In to be more plausible.[116] The Si(111)-$\sqrt{3} \times \sqrt{3}$-Ga structure is also determined as T_4 geometry by LEED analysis.[117] Northrup's energy-minimization calculations for the $\sqrt{3} \times \sqrt{3}$-Al also favor T_4 structure by 0.3 eV/adatom compared with H_3 arrangement if one includes the completely relaxed geometries. Thus the $\sqrt{3} \times \sqrt{3}$ structures on Si(111) surface induced by the group-III metals are now believed to be in the T_4 arrangement (Fig. 36(e)).

Around 0.5 ML and 1 ML coverages, the $\sqrt{31} \times \sqrt{31}$ and 4×1 structures are completed, respectively. But unfortunately there is very little information on the nature of each phase. After the completion of the 4×1 structure, epitaxial growth of ordered In islands is observed at still higher coverages by annealing.[115] Since the dangling bonds are totally saturated in the 4×1 phase, the In adatoms on top of this phase easily moves as revealed by electromigration studies.[118]

5.1.2. *In adsorption and growth*

The initial stage of In adsorption onto the clean Si(111)-7 × 7 surface has been studied with several kinds of experimental methods. Figure 37 shows a series of RHEED patterns with In adsorption. Around 0.3 ML coverage of In (Fig. 37(b)), the relative intensity between the 7 × 7 superlattice reflections changes from that of the clean 7 × 7 surface (Fig. 37(a)); for example, similar intensities of the superspots on the 0th Laue zone in (b) should be compared with those in (a). For the clean 7 × 7 surface, the $(\frac{3}{7}, \frac{3}{7})$-order reflection shows extra intensity which originates from the adatom array with 2 × 2 periodicity in the DAS structure (see Sec. 2.1). Then the intensity distribution of (b) signifies the destruction of periodicity of the adatom arrangement in the 7 × 7 unit. With further adsorption of In, the 7 × 7 super-reflections gradually blur, and finally disappear around 3 or 4 ML coverage. This process seems similar to the Au adsorption case in Fig. 29, but different in the detailed changes in spot intensities.

Figure 38(a) shows the ultraviolet photoemission spectra from the clean Si(111)-7 × 7 surface (dashed curve), and In-covered surfaces (solid lines) with different coverages.[119] The Fermi-level position E_F was determined by linear interpolation of the photoelectric edge of a tantalum sheet in contact to the sample. Since the
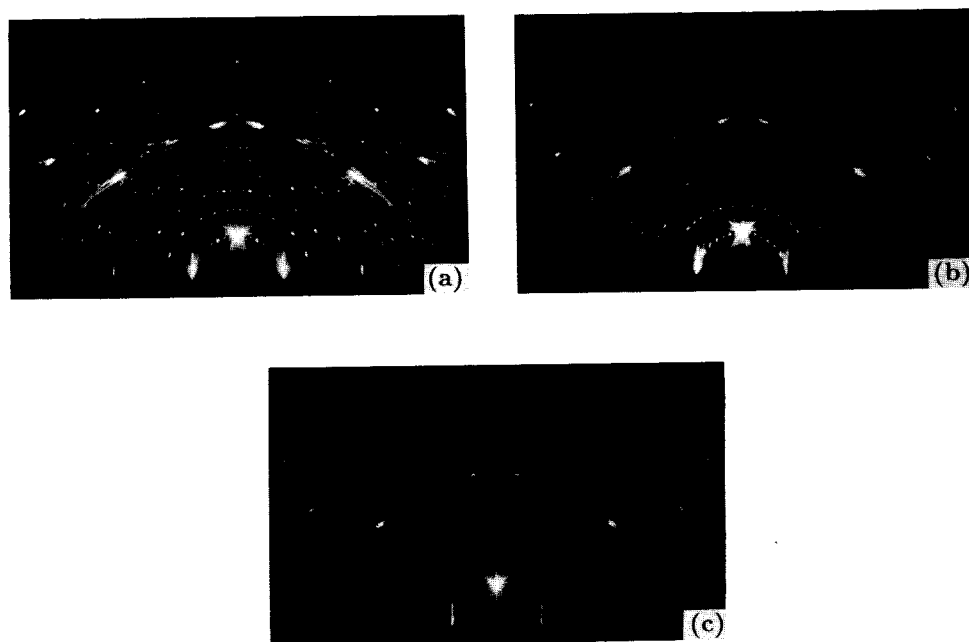

Fig. 37. A series of RHEED patterns during In deposition onto clean Si(111)-7 × 7 surface at RT. In coverages are (a) 0, (b) 0.3, and (c) 1.2 ML. Notice the change in relative intensity ratios between the superlattice spots during blurring out.

peak lying 4.8–5 eV below E_F originates from a feature of the bulk silicon,[120,121] all the curves in the figure are plotted keeping this peak position constant. From these spectra, two facts are noticed. One is that the distance between the bulk-silicon peak and E_F decreases with In coverage. This indicates a change in the relative position of E_F at the surface, which is shown in Fig. 38(b) where the conduction-band minimum (CB) and the vacuum level (VL) referred to E_F are plotted as function of In coverage. The values denoted by CB and VL also correspond to the Schottky barrier height (SBH) and the work function, respectively. The SBH is saturated at 0.95 eV around 3 ML coverage, rather larger than the electrical measurement values ranging between 0.70–0.82 eV. Since the work function ϕ_m of In is 4.2 eV and the electron affinity χ of silicon is between 3.75–4.3 eV,[45] a crude application of Eq. (1) would indicate little or no Schottky barrier formation. So some Fermi-level pinning mechanism is required to actually get the barrier. Another phenomenon
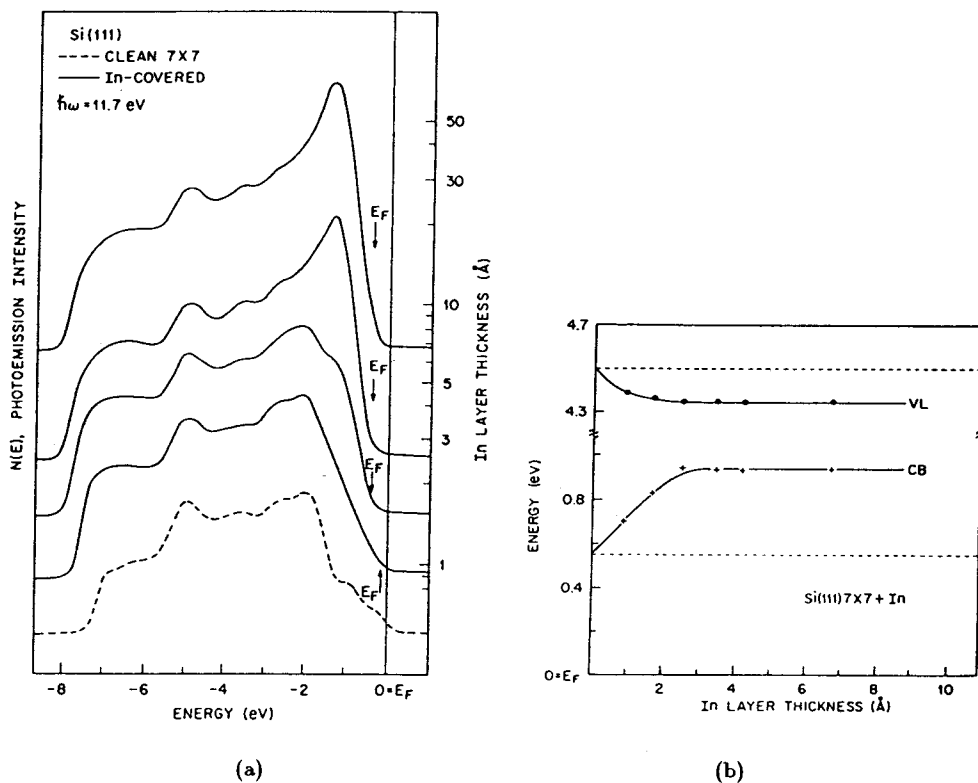

Fig. 38. (a) Ultraviolet photoemission spectra from clean Si(111)-7 × 7 surface (dashed curve) and In-covered surfaces (solid curves) with different coverages.[119] (b) Energy positions of the conduction-band minimum (CB) and the vacuum level (VL) referred to the Fermi level E_F as a function of In coverage, determined by UPS.[119] (c) High-resolution electron-energy-loss spectra taken in sequence of In adsorption onto the clean Si(111)-7 × 7 surface,[122] (d) that for the Si(111)-$\sqrt{3}$ × $\sqrt{3}$-In surface.[123]
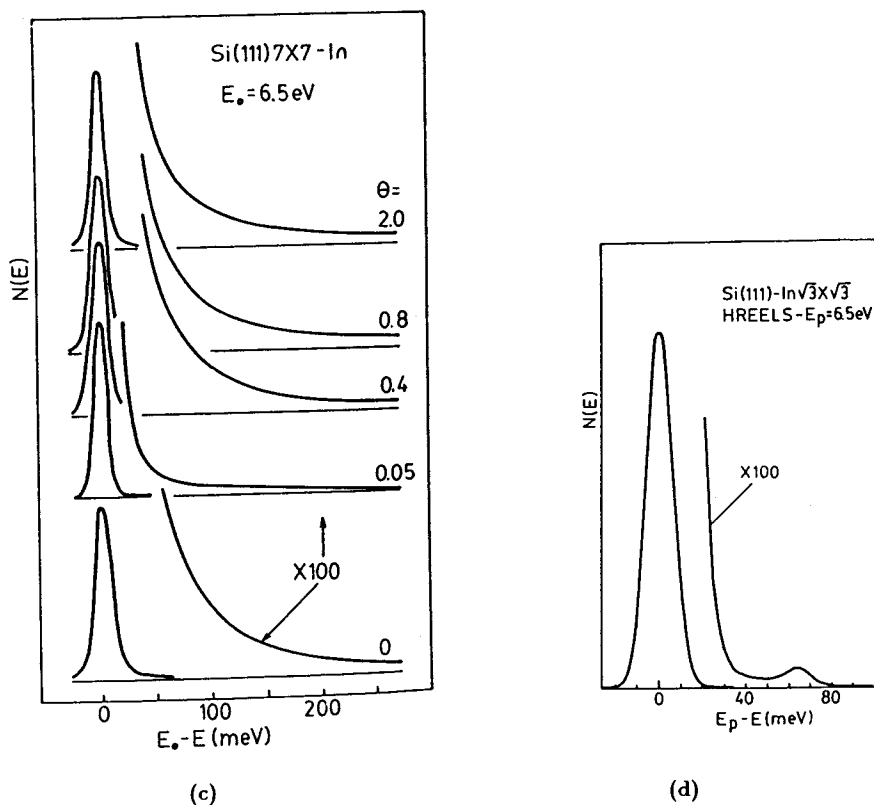
Fig. 38. (*Continued*)

to be noticed in the spectra in Fig. 38(a) is that In of less than 1 ML coverage causes a marked reduction of the density of states near E_F, S_1 and S_2 dangling-bond surface states (see Fig. 3(a)). The first adsorbed In atoms saturate the silicon dangling bonds and metal-induced interface states grow in the valence-band energy region. This process is common to other simple-metal adsorption such as the Ag case shown in Fig. 21(b). This observation leads to a simplistic model of Schottky-Barrier formation that a large density of states exist at E_F for pinning throughout the formation process. The nature of these states type changes from clean-surface type to metal-induced type.

Figure 38(c), (d) show high-resolution electron-energy-loss spectra taken in sequence of In adsorption onto the clean Si(111)-7 × 7 surface (c)[122] and Si(111)-$\sqrt{3}$ × $\sqrt{3}$-In surface (d).[123] The spectrum of the clean 7 × 7 surface has a characteristic tail on the right-hand side of the primary peak, which signifies the metallic nature of the surface. This is contrasted with the spectrum of the $\sqrt{3}$ × $\sqrt{3}$-In surface in Fig. 38(d) where little elastic tail is observed. The metallic tail of the 7 × 7 surface is quickly suppressed by only 0.05 ML In adsorption, corresponding to

the saturation of the dangling bonds of the 7×7 surface. But the metallic character is recovered by further In adsorption of 0.4 ML. Thus the first In adatoms form chemisorption states of covalent bonding with the Si substrate, which evolve into metallic states at coverages of around 1 ML.

Quite different phenomena are observed during the In adsorption onto the pre-deposited substrate, Si(111)-$\sqrt{3} \times \sqrt{3}$-In surface at room temperature. A series of RHEED patterns during In deposition are shown in Fig. 39. Starting from the $\sqrt{3} \times \sqrt{3}$ structure (Fig. 39(a)), 2×2 (b) and $\sqrt{7} \times \sqrt{3}$ (c)(d) phases are completed around 1, 2, and 3 ML, respectively. With further deposition of In, superreflections disappear and only the fundamental spots with streaks from epitaxial In flat islands
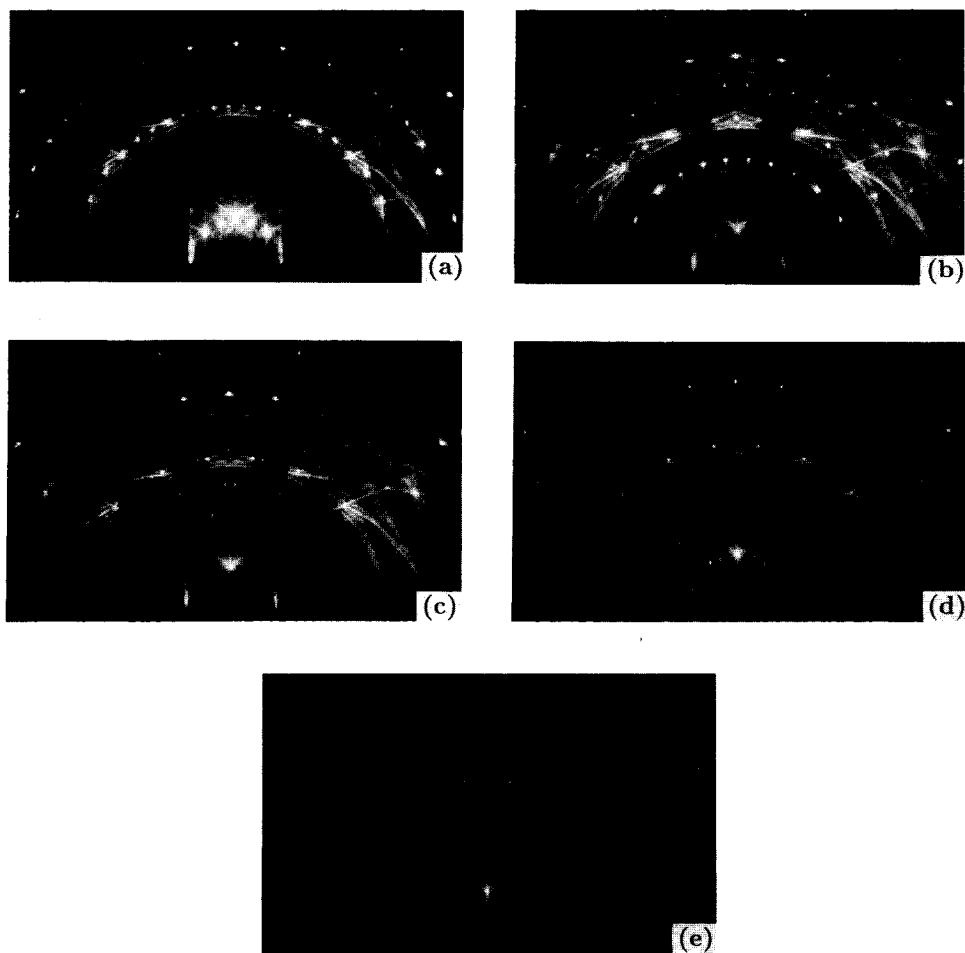

Fig. 39. A series of RHEED patterns during additional In deposition onto Si(111)-$\sqrt{3} \times \sqrt{3}$-In surface at RT. The additional In coverages are (a) 0 ML, (b) 1 ML (2×2), (c) 2 ML ($\sqrt{7} \times \sqrt{3}$), (d) 3 ML ($\sqrt{7} \times \sqrt{3}$), and (e) 4 ML (1×1+In streaks).

are observed in (e). Baba, Zhou and Kinbara[124] mis-indexed the $\sqrt{7} \times \sqrt{3}$ phase as "5 × 5".[125] In the $\sqrt{7} \times \sqrt{3}$ RHEED pattern (d), some superreflection points are observed in a limited range of the electron-beam glancing angle, meaning that this phase is composed of several In atomic layers.[125]

The difference in adsorption process and epitaxial growth between the Si(111)-7 × 7 and Si(111)-$\sqrt{3} \times \sqrt{3}$-In substrates mentioned so far may originate from the presence or absence of the remains of the DAS structure on the topmost layers of the Si substrate. With In adsorption on the UHV-cleaved Si(111)-2 × 1 surface at RT, the surface structure successively changes in a way similar to that for the case of the Si(111)-$\sqrt{3} \times \sqrt{3}$-In substrate; from 2 × 1 into $\sqrt{3} \times \sqrt{3}$, and then 2 × 2.[126] Thus In adatoms move relatively easily to attain a new ordering on normal-stacking Si substrate even at RT, whereas the In-adatom migration may be limited by the remains of the DAS structure on the 7 × 7 substrate.

5.2. *Electrical properties — Surface conductance and Hall effect*

Figure 40 shows the results of simultaneous measurements of the resistance (a) and Hall voltage (b) with a magnetic field of ±340 G during In deposition onto the clean Si(111)-7 × 7 surface (deposition rate = 0.15 ML/min) at RT.[32] The change in RHEED pattern is also indicated in the figure. Both do not show significant changes up to several ML coverage. Even the onset of the conduction through metal islands, which is detected for Ag adsorption (Fig. 16), is not observed in the thicker coverage range. But it is not so curious because In adatoms have a strong tendency to agglomerate into 3D islands even at RT as revealed by a Debye-Scherrer ring pattern in Ref. 124. Since the initial position of the Fermi-level and its shift observed in Fig. 38(b) with In adsorption are almost limited in the depletion range in Fig. 8, conduction through the space-charge layer of the Si substrate is not significantly changed, the resistance remaining almost constant.

In contrast, the In adsorption onto the Si(111)-$\sqrt{3} \times \sqrt{3}$-In at RT causes dramatic changes in resistance and Hall voltage as shown in Fig. 41. With 3 ML coverage the resistance drops down to about one-third of the initial value, and the Hall voltage correspondingly decreases significantly. Large deviations in the Hall voltage data points at the moment of steep drops in resistance are artifacts originated from the inefficient data-processing program for subtracting the zero-level change under zero field. The resistance decrease is not monotonic; synchronized with the structure change at every monolayer growth, the resistance drops almost in steps. After that, the resistance remains constant in spite of the increase of In coverage. The saturation magnitude of the resistance depended on the deposition rate; with a rate of 0.5 ML/min, the final resistance with 3 ML In coverage dropped down to about one-tenth of the initial value. Similar phenomena had been reported by Baba, Zhou, and Kinbara.[124] Since the photoemission data are not available for the sequence of this surface structural change, a detailed discussion can not be made at present. The remarkable and stepwise decrease in resistance, however, is not
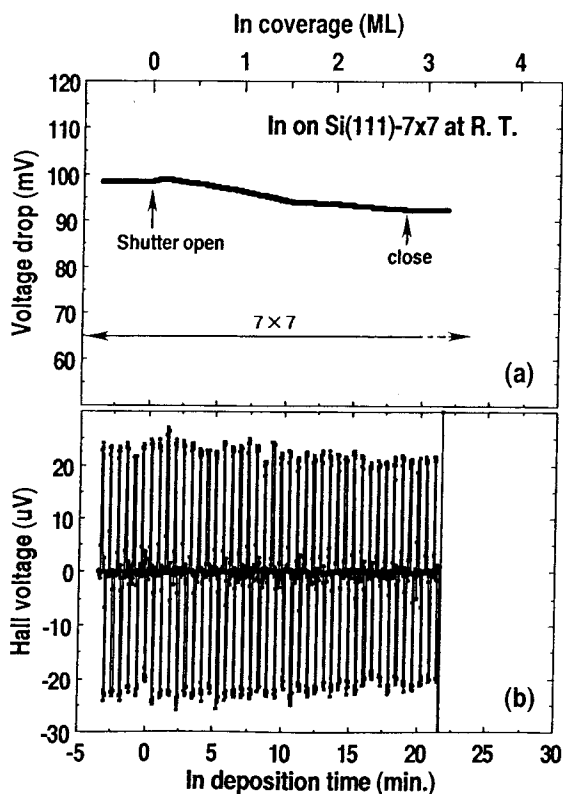
In coverage (ML)

Fig. 40. Changes in (a) resistance and (b) Hall voltage of a Si(111) wafer with 7 × 7 surface at room temperature during In deposition (rate = 0.15 ML/min).[32] The measuring current was 20 μA and a magnetic field of ±340 G was applied.

expected from only the band bending in the Si substrate; the conduction through the grown layer probably also has an important contribution. The conductivity of each phase, $\sqrt{3} \times \sqrt{3}$-In, 2×2-In, or $\sqrt{7} \times \sqrt{3}$-In, may be quite different.

6. Concluding Remarks

Various kinds of experimental and theoretical techniques for surface crystallography and surface electronic-states determination have been proposed, and their availability has been demonstrated through numerous examples of structure analysis. As a direction of future research in surface science, the importance of research on the control of macroscopic properties (electrical, optical, and magnetic properties) combined with structure controls on atomic scales in surface/interface region cannot be over emphasized. Although this theme looks like a fairly device-oriented research, it will be fruitful to tackle this subject from the scientific interests. This approach can lead to a new field of material science which is different from "mesoscopic" physics.
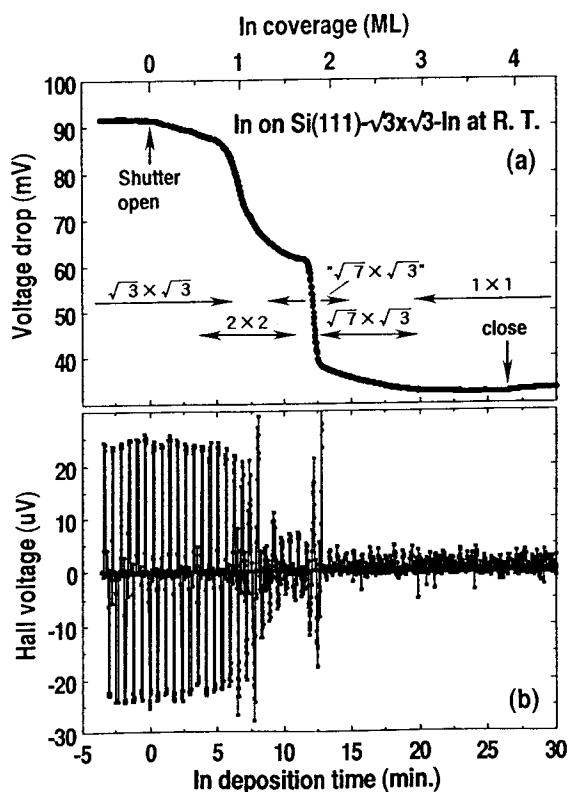
Fig. 41. Changes in (a) resistance and (b) Hall voltage of a Si(111) wafer with $\sqrt{3} \times \sqrt{3}$-In surface at room temperature during In deposition (rate = 0.15 ML/min).[32] The measuring current was 20 μA and a magnetic field of ±340 G was applied.

In the present review we have collected the reports from this point of view. We hope this kind of work will attract growing interest from researchers in the fields of surface science and semiconductor physics.

Acknowledgments

References

1. For a review, D. Haneman, *Rep. Prog. Phys.* **50**, 1045 (1987).
2. K. Takayanagi, Y. Tanishiro, M. Takahashi, and S. Takahashi, *J. Vac. Sci. Technol.* **A3**, 1502 (1985); *Surf. Sci.* **164**, 367 (1985).
3. For a review, G. V. Hansson and R. I. G. Uhrberg, *Surf. Sci. Rep.* **9**, 197 (1988).
4. R. J. Hamers, R. M. Tromp and J. E. Demuth, *Phys. Rev. Lett.* **56**, 1972 (1986).
5. T. Takahashi, S. Nakatani, N. Okamoto, T. Ishikawa, and S. Kikuta, *Jpn. J. Appl. Phys.* **27**, L753 (1988); *Surf. Sci.* **242**, 54 (1991).

6. T. Takahashi and S. Nakatani, *Proc. 8th Int. Conf. on Solid Surfaces* (The Hague, 1992) (*Surf. Sci.*, in press).
7. For a review, see *Reflection High-Energy Electron Diffraction and Reflection Electron Imaging of Surfaces*, ed. P. K. Larson and P. J. Dobson (Plenum, New York, 1988).
8. R. S. Becker, J. A. Golovchenko and B. S. Swartzentruber, *Nature* **325**, 419 (1987).
9. D. M. Eigler and E. K. Schweizer, *Nature* **344**, 524 (1990); D. M. Eigler, C. P. Lutz and W. E. Rudge, *Nature* **352**, 600 (1991).
10. For example, *Metallization and Metal-Semiconductor Interfaces*, ed. I. P. Batra (Plenum, New York, 1988).
11. For a review, see L. J. Brillson, *Surf. Sci. Rep.* **2**, 123 (1982).
12. F. Bechstedt and R. Enderlein, *Semiconductor Surfaces and Interfaces* (Akademie-Verlag, Berlin, 1988), Chap. 4.
13. W. Schottky, *Naturwissenschaften* **26**, 843 (1938).
14. N. F. Mott, *Proc. Cambridge Phil. Soc.* **34**, 568 (1938).
15. T. Hibma, H. H. Weitering, D. R. Heslinga, and T. M. Klapwijk, *Appl. Surf. Sci.* **48/49**, 209 (1991).
16. V. Heine, *Phys. Rev.* **A138**, 1689 (1965).
17. J. Tersoff, *Phys. Rev. Lett.* **52**, 465 (1984).
18. W. E. Spicer, P. W. Chye, P. R. Skeath, and I. Lindau, *J. Vac. Sci. Technol.* **16**, 1422 (1979).
19. W. Mönch, *Appl. Surf. Sci.* **41/42**, 128 (1989); *Phys. Rev. Lett.* **58**, 1260 (1987).
20. R. T. Tung, *Phys. Rev. Lett.* **52**, 461 (1984).
21. S. Chang, L. J. Brillson, Y. J. Kime, D. S. Rioux, P. D. Kirchner, G. D. Petit, and J. M. Woodall, *Phys. Rev. Lett.* **64**, 2551 (1990).
22. G. LeLay, K. Hricovini and J. E. Bonnet, *Appl. Surf. Sci.* **41/42**, 25 (1989).
23. D. R. Heslinga, H. H. Weitering, D. P. van der Werf, T. M. Klapwijk, and T. Hibma, *Phys. Rev. Lett.* **64**, 1589 (1990).
24. H. H. Weitering, A. R. H. F. Ettema and T. Hibma, *Phys. Rev.* **B45**, 9126 (1992).
25. H. H. Weitering, J. P. Sullivan, R. J. Carolissen, W. R. Graham, and R. T. Tung, *Proc. 8th Int. Conf. on Solid Surfaces* (The Hague, 1992) (*Appl. Surf. Sci.* in press).
26. A. Many, Y. Goldstein and N. B. Grover, *Semiconductor Surfaces* (North-Holland, Amsterdam, 1965).
27. D. R. Frankl, *Electrical Properties of Semiconductor Surfaces* (Pergamon, Oxford, 1967).
28. M. Henzler, in *Surface Physics of Materials I*, ed. J. M. Blakely (Academic Press, New York, 1975), p. 241.
29. S. Hasegawa and S. Ino, *Phys. Rev. Lett.* **68**, 1192 (1992).
30. S. Hasegawa and S. Ino, *Proc. 3rd Int. Symp. on Dynamical Processes at Solid Surfaces* (Tokyo, 1992), ed. K. Terakura and Y. Murata [*Surf. Sci.* **283**, 438 (1993)].
31. S. Hasegawa and S. Ino, *Proc. 8th Int. Conf. on Solid Surfaces* (The Hague, 1992) (*Thin Solid Films*, in press).
32. S. Hasegawa and S. Ino, *Jpn. J. Appl. Phys.* to be published.
33. D. Haneman, *Adv. Phys.* **31**, 165 (1982).
34. G. X. Qian and D. J. Chadi, *J. Vac. Sci. Technol.* **B4**, 1079 (1986).
35. G. X. Qian and D. J. Chadi, *Phys. Rev.* **B35**, 1288 (1987).
36. S. Ino, *Jpn. J. Appl. Phys.* **16**, 891 (1977).
37. A. Ishizaka and Y. Shiraki, *J. Electrochem. Soc.* **133**, 666 (1986).
38. S. Ino, *Jpn. J. Appl. Phys.* **19**, L61, 1277 (1980).
39. H. Daimon and S. Ino, *Surf. Sci.* **164**, 320 (1985).
40. Y. Horio, A. Ichimiya, S. Kohmoto, and H. Nakahara, *Surf. Sci.* **257**, 167 (1991).

41. H. Nakahara and A. Ichimiya, *J. Cryst. Growth* **99**, 514 (1990).
42. J. E. Demuth, B. N. J. Persson and A. J. Schell-Sorokin, *Phys. Rev. Lett.* **51**, 2214 (1983).
43. J. E. Northrup, *Phys. Rev. Lett.* **57**, 154 (1986).
44. F. J. Himpsel, G. Hollinger and R. A. Pollack, *Phys. Rev.* **B28**, 7014 (1983).
45. S. M. Sze, *Physics of Semiconductor Devices* (John Wiley, New York, 1981).
46. W. Mönch, p. 11 in Ref. 10.
47. J. Bardeen, *Phys. Rev.* **71**, 717 (1947).
48. For a review, W. Mönch, *Surf. Sci.* **182**, 92 (1983).
49. H. B. Michaelson, *J. Appl. Phys.* **48**, 4729 (1977).
50. H. B. Michaelson, *IBM J. Res. Dev.* **22**, 72 (1978).
51. J. Vrijmoeth, J. F. van der Veen, D. R. Heslinga, and T. M. Klapwijk, *Phys. Rev.* **B42**, 9598 (1990).
52. G. Le Lay and K. Hricovini, *Phys. Rev. Lett.* **65**, 807 (1990).
53. H. H. Weitering, D. R. Heslinga, T. Hibma, and T. M. Klapwijk, *Phys. Rev. Lett.* **65**, 808 (1990).
54. J. A. Carlisle, T. Miller and T. -C. Chiang, *Phys. Rev.* **B45**, 3400 (1992).
55. C. E. Young, *J. Appl. Phys.* **32**, 329 (1961).
56. R. H. Kingston and S. F. Neustadter, *J. Appl. Phys.* **26**, 718 (1955).
57. P. Blood and J. W. Orton, *The Electrical Characterization of Semiconductor: Majority Carriers and Electron States* (Academic, New York, 1992).
58. W. H. Brattain and J. Bardeen, *Bell System Tech. J.* **32**, 1 (1953).
59. S. R. Morrison, *J. Phys. Chem.* **57**, 860 (1953).
60. J. Bardeen and S. R. Morrison, *Physica* **20**, 873 (1954).
61. J. V. Wienskowski and W. Mönch, *Phys. Stat. Sol. (b)* **45**, 583 (1971).
62. F. Bäuerle, W. Mönch and M. Henzler, *J. Appl. Phys.* **43**, 3917 (1972).
63. P. P. Auer and W. Mönch, *Japan. J. Appl. Phys. Suppl. 2, Pt. 2*, 397 (1974).
64. W. Mönch, *Surf. Sci.* **63**, 79 (1977).
65. K. Spiegel, *Surf. Sci.* **7**, 125 (1967).
66. E. L. Bullock, G. S. Herman, M. Yamada, D. J. Friedman, and C. S. Fadley, *Phys. Rev.* **B41**, 1703 (1990).
67. M. Katayama, R. S. Williams, M. Kato, E. Nomura, and M. Aono, *Phys. Rev. Lett.* **66**, 2762 (1991).
68. Y. G. Ding, C. T. Chan and K. M. Ho, *Phys. Rev. Lett.* **67**, 1454 (1991).
69. S. Watanabe, M. Aono and M. Tsukada, *Phys. Rev.* **B44**, 8330 (1991).
70. T. Yokotsuka, S. Kono, S. Suzuki, and T. Sagawa, *Surf. Sci.* **127**, 35 (1983).
71. J. M. Nicholls, F. Salvan and B. Reihl, *Phys. Rev.* **B34**, 2945 (1986).
72. S. Kono, K. Higashiyama, T. Kinoshita, T. Miyahara, H. Kato, H. Ohsawa, Y. Enta, F. Maeda, and Y. Yaegashi, *Phys. Rev. Lett.* **58**, 1555 (1987).
73. L. S. O. Johansson, E. Landemark, C. J. Karlsson, and R. I. G. Uhrberg, *Phys. Rev. Lett.* **63**, 2092 (1989).
74. Y. Goto and S. Ino, *Jpn. J. Appl. Phys.* **17**, 2097 (1978); *Thin Solid Films* **109**, 255 (1983).
75. G. LeLay, M. Manneville and R. Kern, *Surf. Sci.* **72**, 405 (1978).
76. G. LeLay, *Surf. Sci.* **132**, 169 (1983).
77. M. Saitoh, F. Shoji, K. Oura, and T. Hanawa, *Surf. Sci.* **112**, 306 (1981).
78. Y. Terada, T. Yoshizuka, K. Oura, and T. Hanawa, *Surf. Sci.* **114**, 65 (1982).
79. T. Ichikawa and S. Ino, *Surf. Sci.* **97**, 489 (1980).
80. G. LeLay, A. Chauvet, M. Manneville, and R. Kern, *Appl. Surf. Sci.* **9**, 190 (1980).
81. S. Hasegawa, H. Daimon and S. Ino, *Surf. Sci.* **186**, 138 (1987).

82. R. J. Wilson and S. Chiang, *Phys. Rev. Lett.* **58**, 369 (1987).
83. W. C. Fan and A. Ignatiev, *Phys. Rev.* **41**, 3592 (1990).
84. E. Bauer and H. Poppa, *Thin Solid Films* **12**, 167 (1972).
85. M. Hanbüchen, M. Futamoto and J. A. Venales, *Surf. Sci.* **147**, 433 (1984).
86. Y. Gotoh, S. Ino and H. Komatsu, *J. Cryst. Growth* **56**, 498 (1982).
87. St. Tosch and H. Neddermeyer, *Phys. Rev. Lett.* **61**, 349 (1988).
88. H. Neddermeyer, *Critical Reviews in Solid State and Materials Sciences* **16**, 309 (1990).
89. St. Tosch and H. Neddermeyer, *J. Microscopy*, **152**, 415 (1988).
90. H. Hong, R. D. Aburano, D. S. Lin, H. Chen, and T. C. Chiang, *Phys. Rev. Lett.* **68**, 507 (1992).
91. A. Samsavar, T. Miller and T. C. Chiang, *Phys. Rev.* **B42**, 9245 (1990).
92. Y. Borensztein and R. Alameh, *Surf. Sci. Lett.* **274**, L509 (1992).
93. R. T. Tung, *Phys. Rev.* **B45**, 13509 (1992).
94. L. Braicovich, I. Abbati, J. N. Miller, I. Lindau, S. Schwarz, P. R. Skeath, C. Y. Su, and W. E. Spicer, *J. Vac. Sci. Technol.* **17**, 1005 (1980).
95. A. Hiraki, *Surf. Sci. Rep.* **3**, 357 (1984).
96. S. L. Molodtsov, C. Laubschat, A. M. Shikin, and V. K. Adamchuk, *Surf. Sci.* **269/270**, 988 (1992).
97. S. Ino, *Butsuri* **37**, 82 (1982) (in Japanese).
98. S. Ino, p. 3 in Ref. 7.
99. S. Takahashi, Y. Tanishiro and K. Takayanagi, *Surf. Sci.* **242**, 73 (1991).
100. K. Higashiyama, S. Kono and T. Sagawa, *Jpn. J. Appl. Phys.* **25**, L117 (1986).
101. A. A. Baski, J. Nogami and C. F. Quate, *Phys. Rev.* **B41**, 10247 (1990).
102. H. Lipson and K. E. Singer, *J. Phys.* **C7**, 12 (1974).
103. H. Daimon, C. Chung, S. Ino, and Y. Watanabe, *Surf. Sci.* **235**, 142 (1990).
104. E. Bauer, *Surf. Sci. Lett.* **250**, L379 (1991).
105. T. Hasegawa, K. Takada, S. Hosaka, and S. Hosoki, *J. Vac. Sci. Technol.* **A8**, 241 (1990).
106. J. Nogami, A. A. Baski and C. F. Quate, *Phys. Rev. Lett.* **65**, 1611 (1990).
107. Y. Tezuka, Ph. D. thesis, 1991, University of Tokyo.
108. R. I. G. Uhrberg, G. V. Hansson, U. O. Karlsson, J. M. Nicholls, P. E. S. Persson, S. A. Flodstorm, R. Engelhardt, and E. E. Koch, *Phys. Rev.* **B31**, 3795 (1985).
109. C. J. Karlsson, E. Landemark, L. S. O. Johansson, and R. I. G. Uhrberg, *Phys. Rev.* **B42**, 9546 (1990).
110. J. J. Lander and J. Morrison, *Surf. Sci.* **2**, 553 (1964).
111. S. Baba, M. Kawaji and A. Kinbara, *Surf. Sci.* **85**, 29 (1979); T. Aiyama and S. Ino, *Surf. Sci.* **82**, L585 (1979).
112. J. E. Northrup, *Phys. Rev. Lett.* **53**, 683 (1984).
113. J. M. Nicholls, P. Mårtensson, G. V. Hansson, and J. E. Northrup, *Phys. Rev.* **32**, 1333 (1985).
114. G. V. Hansson, J. M. Nicholls, P. Mårtensson, and R. I. G. Uhrberg, *Surf. Sci.* **168**, 105 (1986).
115. J. Nogami, S. Park and C. F. Quate, *Phys. Rev.* **B36**, 6221 (1987).
116. K. Izumi, T. Takahashi and S. Kikuta, *Jpn. J. Appl. Phys.* **28**, 1742 (1989).
117. A. Kawazu and H. Sakama, *Phys. Rev.* **B37**, 2704 (1988).
118. H. Yasunaga, Y. Kubo and N. Okuyama, *Jpn. J. Appl. Phys.* **25**, L400 (1986).
119. G. Margaritondo, J. E. Rowe and S. B. Christman, *Phys. Rev.* **B14**, 5396 (1976).
120. J. E. Rowe and H. Ibach, *Phys. Rev. Lett.* **32**, 421 (1974).

121.   E. O. Kane, *Phys. Rev.* **146**, 558 (1966).

122.   M. K. Kelly, E. Colavita, G. Margaritondo, J. Anderson, L. Papagno, D. J. Frankel, and G. J. Lapeyre, *Phys. Rev.* **B32**, 2693 (1985).

123.   M. K. Kelly, G. Margaritondo, J. Anderson, D. J. Frankel, and G. J. Lapeyre, *J. Vac. Sci. Technol.* **A4**, 1396 (1986).

124.   S. Baba, J. M. Zhou and A. Kinbara, *Jpn. J. Appl. Phys.* **19**, L571 (1980).

125.   T. Tsuno, Ph. D. thesis, 1990, University of Tokyo.

126.   D. Bolmont, P. Chen, C. A. Sébenne, and F. Proix, *Surf. Sci.* **137**, 280 (1984).

127.   S. Hasegawa, Y. Nagai, T. Oonishi, and S. Ino, *Phys. Rev.* **B47**, 9903 (1993).